

POLITECNICO DI TORINO

LEVEL's Degree in Physics of Complex Systems



LEVEL's Master Degree Thesis

**Theory and Simulations of Microcavity
Dissipative Kerr Solitons in the presence
of Mode Interactions with Applications to
Low-Noise Microwave Generation**

Supervisors

Prof. Tobias J. KIPPENBERG

Prof. Vittorio PENNA

Dr. Alexey TIKAN

Candidate

Andrea Carmelo TRISCARI

22/07/2022

Abstract

Optical Kerr microresonators in the last years have acquired attention from the scientific community, being from a fundamental point of view rich complex physical systems but at the same time, thanks to the late improvements of the nanofabrication technologies, feasible to fabricate in a controlled way. That has recently resulted in a plethora of cutting-edge applications spanning from spectroscopy to LIDAR and atomic clocks. The complex behaviour of the optical field within the resonator arises from being both an out-of-equilibrium and nonlinear system, leading to the emergence of bistability, hysteresis of the optical resonance, chaotic behaviour, and self-organization in coherent states. This dynamics is accurately described by the Lugiato-Lefever equation, a generalization of the Nonlinear Schrödinger equation accounting for further driven-dissipative terms. Among the different attractor state of the system, there is one essential for the majority of the applications of these devices, so-called Dissipative Kerr Soliton (DKS), a stable, coherent and localized state circulating inside the cavity. Despite its stability, its generation in the resonator can be inhibited by the presence of interactions between different cavity mode families due to non-ideal geometry and parasitic scattering centers. That gives birth to the so-called avoided mode crossings (AMX), that lead to the generation of dispersive waves that can destabilize or completely forbid the formation of DKS. Moreover, the presence of the interaction between the confined light and the vibrational degrees of freedom of the material, known as Raman scattering, further reduces the stability of the DKS and makes it sensitive to the driver noise. The generation of noiseless soliton is one of the essential ingredient to obtain state-of-the-art integrated photonics devices. Recent experimental studies found out that in presence of AMX, the soliton response to the driver noise can be substantially reduced. In this framework, the aim of the thesis is to deepen the understanding of the phenomenon of noise reduction, by deriving a perturbed Lugiato-Lefever model – in a form of complex nonlinear partial differential equation (PDE) - that embodies both the generation of dispersive waves, key properties of AMX, and Raman scattering. The nonlinear dynamics of the model has been simulated and the properties of the generated solitons have been studied through Lagrangian perturbative approach, obtaining conditions for the minimization of the noise dependence.

Acknowledgements

I would like to thank Polytechnic of Turin for the scientific education he conveyed to me through the hard work of the professors of the course in Physics of Complex Systems.

I want also to thank Professor Tobias J.Kippenberg for the opportunity offered to me to join his Lab to work on this thesis project.

Thank you also to Alexey and Sasha, for the support given both for this work.

(In italian for my family) Voglio inoltre ringraziare la mia famiglia, i miei genitori e le mie sorelle che mi hanno sempre supportato e sopportato, specialmente in questi ultimi anni in cui sarei potuto essere piu' vicino. Ai miei genitori dedico questo lavoro, ringraziandoli per avermi dato la possibilita' di studiare fuori casa, e di farmi arrivare fin qui. Un ringraziamento speciale non puo' mancare alla Nonna Franca, che seppur a distanza in questi anni, l'ho sentita sempre vicina col pensiero e con le sue preghiere giornaliere.

Table of Contents

List of Figures	VI
1 Introduction to Kerr Microresonators	1
1.1 Platform and Applications	1
1.1.1 Physical properties of the system	3
1.1.2 Coupled-mode and Lugiato Lefever equations	4
1.1.3 Realistic Dispersion Profile and limits of the equation: Higher order Dispersion and Avoided Mode Crossing	6
2 Model of the Avoided Mode Crossing	10
2.1 Perturbed LLE	10
2.2 Properties of the Equation and Conservation Laws	11
2.2.1 Continuity equation for the Norm	11
2.2.2 Dynamics of the Momentum	12
2.2.3 Symmetries of the Equation	14
2.2.4 Case $\mu = 0$	15
2.2.5 Case $\mu \neq 0$	16
2.3 Simulations	17
2.3.1 Dimensionality of parameter space and choice of the pump power	17
2.3.2 Case $\bar{\mu} = 0$	17
2.3.3 Case $\bar{\mu} \neq 0$	18
3 Noise reduction and Microwave generation	23
3.1 Noise transduction mechanism	24
3.2 Extension of the model: Detuning Noise	25
3.2.1 Simulated Soliton Dynamics in Presence of Noise	26
3.3 Extension of the model: Raman Scattering	29
3.4 Quiet Point	31
3.5 Alternative approach to QP	33
3.5.1 Results	34

3.5.2	Analytical Derivation	39
4	Numerical Methods	45
4.1	Split-Step Algorithm	45
4.2	Simulation of perturbed LLE	47
4.2.1	Hard and Soft Seed	48
4.2.2	Faraday Instability	49
4.2.3	Soliton Noisy dynamics simulation	50
4.3	Newton-Raphson Method	50
4.4	General description of the method	51
4.4.1	Soliton Group Velocity Implementation: Equations	52
4.4.2	Matrix Form of the Equations	54
4.4.3	Discretization of the Equations	56
4.4.4	Initialization condition	59
5	Conclusions and outlook.	61
	Bibliography	63

List of Figures

1.1	Applications of Kerr microresonators (figure adapted from [2]). . . .	2
1.2	Schematic representation of kerr microresonator (figure adapted from [2]).	3
1.3	Stability Diagram of Lugiato-Lefever equation (figure adapted from [22]). From the figure we can see the stable attractors of the system in dependence of the operating point. With stable MI is intended stable Modulation instability, that is the phenomena by which the homogeneous solution becomes unstable due to four-wave mixing processes, that in an ordered way start occupying more resonating cavity modes, forming the so called Turing rolls, whose spatial profile is visible in the figure. If the detuning ζ_0 is further increased, the system enters in the region of Chaotic MI, where now the resonating modes are occupied in a chaotic way, destabilizing Turing rolls, obtaining a unstructured field distribution inside the resonator. At the end of this region, the breathers or solitons regions are reached, where localized structured becomes stable. See [20] for further details.	6
1.4	Example of Avoided mode crossing interaction. We can see how the dispersions of two modes belonging to different family, interacts avoiding the crossing. Furthermore from the mode profile is possible to see that in the neighborhood of the crossing the two modes hybridize.	8
1.5	Example of a realistic dispersion profile in presence of Avoided mode crossing interaction, figure adapted from [23].	8
2.1	Tuning to resonance for different resonance shift $\bar{\mu} = 0$. a) No resonance shift, b) $a_{\bar{\mu}} = 3$, c) $a_{\bar{\mu}} = 5$, d) $a_{\bar{\mu}} = 10$. e) No resonance shift, f) $a_{\bar{\mu}} = -3$, g) $a_{\bar{\mu}} = -5$, h) $a_{\bar{\mu}} = -10$. We can see that according to the strength of the resonance shift the system is found in a different region of the parameter space, as already verified in [39]	19

2.2	Single soliton simulated dynamics. We can see the simulated soliton (light green line) propagating along the azimuthal coordinate θ during time t for the operating point $(\zeta_0, a_{\bar{\mu}}, \bar{\mu}) = (4, -8, 6)$. Both the modulation of the background and the presence of periodic boundary conditions are visible.	20
2.3	Dissipative cavity soliton. Simulated soliton for $\bar{\mu} = 18$. As already demonstrated, the period is related to the mode number, such that there are exactly 18 "hills" in the dispersive tail of the soliton. . . .	20
2.4	Solitons in real space and their spectra for different resonance shifts $a_{\bar{\mu}}$.	21
2.5	Soliton Crystal state. Soliton crystal state, $(a_{\bar{\mu}} = -0.66, \bar{\mu} = 15)$. We can see how the period (i.e. lattice length) is exactly equal to the number of mode displaced, this due to the presence of the modulated background.	21
2.6	Periodicity of the soliton background Different stable soliton solution for different mode number $\bar{\mu}$ displaced.	22
2.7	$P-\mu$ Symmetry We can clearly see from the figures how the dynamics for two operating points in the parameters (sub)space $(\zeta_0, a_{\bar{\mu}}, \bar{\mu})$ -plane, differing only for the value of $\bar{\mu}$, equal to $\bar{\mu} = 6$ (left) and $\bar{\mu} = -6$ (right), is related by a parity transformation.	22
3.1	Simulated soliton dynamics in presence of sinusoidal modulation of the detuning. $\bar{m} = 15, f^2 = 6, \zeta_0 = 4, \delta\zeta(t) = 0.1\zeta_0 \cos(\alpha t + \varphi), \alpha = 0.0033, \varphi = -200$. a) Detuning b) (log scale) Real space soliton dynamics: we can see that the soliton and the dispersive wave are phase locked, responding coherently to the noise. c) Response of the soliton in Fourier space: The linear dispersion of the soliton change angle periodically, following the detuning change. d) Zoom of the linear dispersion: we can see how the presence of the modulated background for different detuning shows that at any detuning the soliton dispersion is phase matched with the displaced resonance of mode $\bar{\mu}$	28
3.2	Simulated soliton dynamics in presence of random noise and single mode displaced only. $\bar{m} = 15, f^2 = 6, \zeta_0 = 4$ a) Stochastic Detuning b) (log scale) Real space soliton dynamics c) Response of the soliton in Fourier space	29
3.3	Simulation of soliton dynamics in presence of Sinusoidal noise and Raman scattering only. The noise is exactly the same sinusoidal noise as in figure 3.1 but with only Raman scattering present. No resonance for any particular mode indeed and absence of dispersive wave.	31

3.4	Simulation of soliton dynamics in presence of random Lorentian noise and Raman scattering only. Simulation of soliton dynamics in presence of the same random noise as in figure 3.2 but with only Raman scattering present. No resonance for any particular mode indeed and absence of dispersive wave.	31
3.5	Comparison of noise cancellation for different operating points. a) Simulated soliton dynamics in presence of detuning random noise and Raman scattering only. b),c),d),e) Simulated soliton dynamics in presence of exactly the same realization of the random detuning noise present in figure a, computed at different operating points, differing only by the mode number $\bar{\mu}$, in alphabetical order: $\bar{\mu} = 10$, $\bar{\mu} = 21$, $\bar{\mu} = -10$, $\bar{\mu} = -21$	33
3.6	Computed soliton group velocities and occupancy of displaced mode in $(\zeta_0, a_{\bar{\mu}})$-subspace with Newton-Raphson method a)Soliton group velocity for $(\zeta_0, a_{\bar{\mu}}), \bar{\mu} = -21$, b)Soliton group velocity for $(\zeta_0, a_{\bar{\mu}}, \bar{\mu} = 21)$, c)Occupancy of displaced mode for $(\zeta_0, a_{\bar{\mu}}, \bar{\mu} = -21)$, d)Occupancy of displaced mode for $(\zeta_0, a_{\bar{\mu}}, \bar{\mu} = 21)$. We can see that the group velocity and the occupancy of the displaced mode $\bar{\mu}$ present a similar behaviour. To note that, due to the presence of Raman term, we have the breaking of $P - \mu$ -symmetry obtaining that $v_{g,\bar{\mu}>0} \neq -v_{g,\bar{\mu}<0}$	35
3.7	Example of fixed detuning lines for derivative computation in the case of subfigure a) of fig. 3.6	36
3.8	Directional derivative of soliton group velocity along the ζ_0-direction (i.e. detuning). \log_{10} value of the directional derivatives along the detuning direction of the group velocities of figure 3.6, with subfigures in the same order. It is clear the difference between positive and negative mode, since the latter present a further line of quiet points.	36
3.9	Choosing the operating points on the group velocity change plot for further investigation of the noise properties.	38
3.10	Resulting simulations related to fig.3.9	39
3.11	Comparison between the numerical (left) and analytical (right) values of the log-derivative of the group velocity.	43
3.12	Comparison between the numerical (left) and analytical (right) 3D plots of the soliton (log-)group velocity $\log_{10}(\partial_{\zeta_0} v_g)$ We can see how the analytical formula predicts the different behaviours for opposite values of $\bar{\mu}$	44

Chapter 1

Introduction to Kerr Microresonators

1.1 Platform and Applications

In the latest years the world of photonic integrated circuits (PIC) has attracted much more attention thanks to the improvements of the nanofabrication processes that made possible to produce very small PIC, very precisely. In particular, a big contribution to the recent success of the integrated photonics is undoubtedly represented by the Kerr microresonators, systems at the boarder between pure physical experiments from one side, due to the interplay between nonlinear and out-of-equilibrium dynamics that lead to the emergence of numerous exotic features, and from the another side they represent actual photonics devices with a wide range of applications. The key features of these devices is represented by their capability of generating dissipative Kerr solitons (DKS) [1] and consequently optical frequency combs [2]. The latter have revolutionised over the past two decades our ability to accurately frequency calibration and led to numerous advances, such optical atomic clocks and were awarded the 2005 Nobel Prize in Physics.

The discovery of solitons in microresonators has unlocked the full potential of the integrated photonics: within only few years, soliton microcombs have been used in a variety of system level demonstrations [2], in the field of telecommunications, connecting the microwave and optical regimes [3, 4], creating optical frequency synthesizers [5], enhancing parallel coherent communications [6], in the field of measurements and sensors, with the implementation of dual-comb spectroscopy [7], LIDAR [8, 9], Low-noise microwave generation [10] and astronomical spectroscopy [11, 12]. In this way, soliton microcombs have become a new research field worldwide at the interface of frequency metrology, soliton physics and nonlinear dynamics with integrated photonics. DKSs are formed by non-equilibrium optical

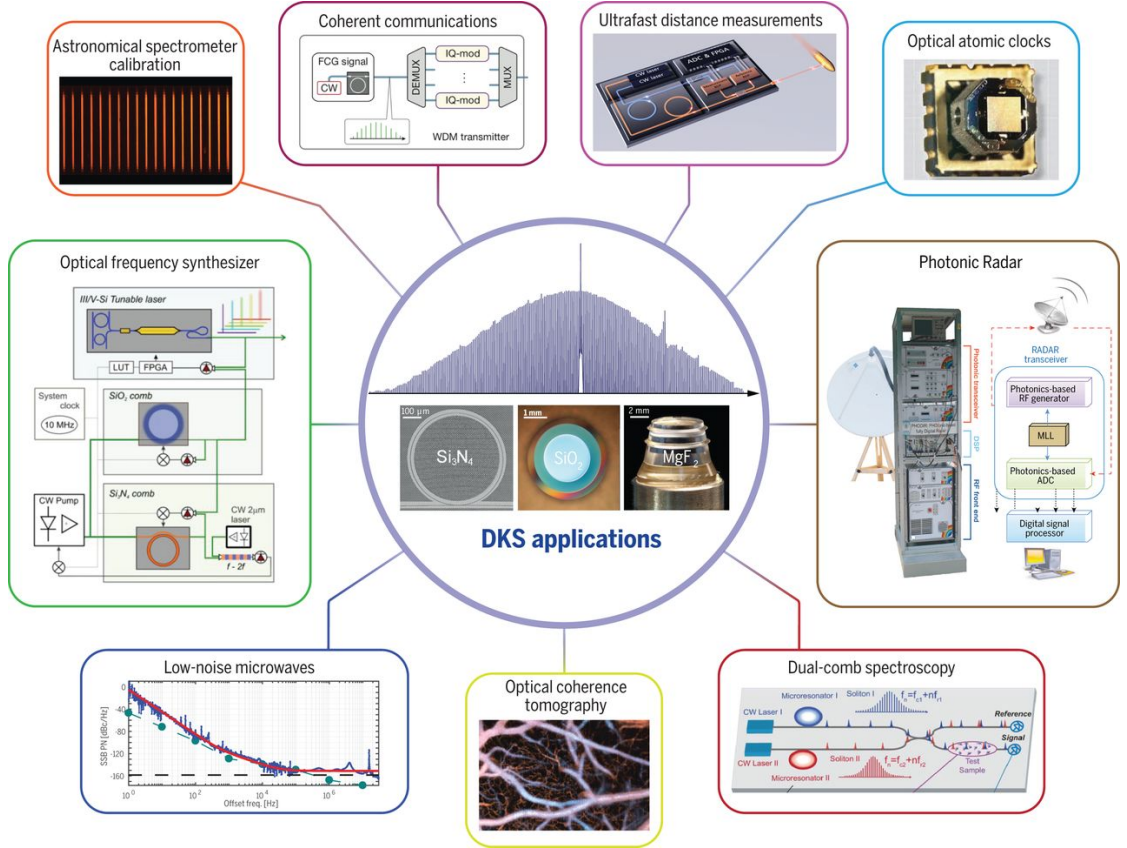


Figure 1.1: Applications of Kerr microresonators (figure adapted from [2]).

driving, and represent a double balance between chromatic dispersion and Kerr nonlinearity, as well as cavity losses and parametric gain.

The simplest implementation of a Kerr microresonator is the one shown in Fig. 1.2, in which the resonator is represented by a single ring of dielectric material (usually of Si_3N_4) that can support resonating optical modes. These are excited through an external light source, usually a tunable continuous wave (CW) laser, coupled to the ring through an external waveguide made of the same material. The nature of the coupling has to be assigned to the spatial overlap of the mode volume of the input field with one (or more) resonant modes of the cavity, and so its strength, usually parameterized by the parameter κ_{ex} , can be opportunely engineered by fabrication design. Since the nature of the coupling is usually not directional, as the input field is coupled inside the resonator, at the same time part of the intracavity field is outcoupled to the external waveguide. And from that the DKS (i.e. frequency comb) is measured.

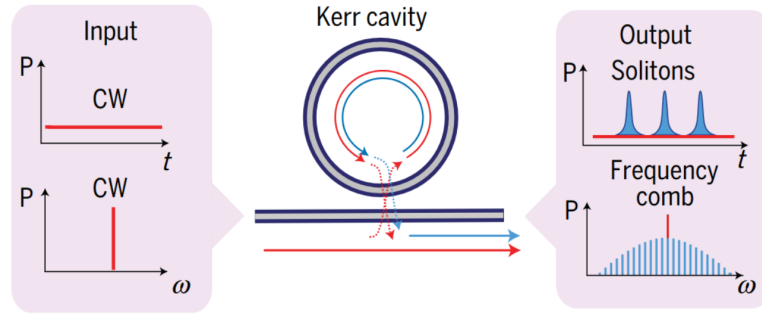


Figure 1.2: Schematic representation of Kerr microresonator (figure adapted from [2]).

1.1.1 Physical properties of the system

The richness of the features that an already (relative) simple implementation like 1.2 can manifest, is due to the properties of the dielectric (Si_3N_4), being an absorbent, nonlinear and dispersive material.

Being absorbent it means that, while the light circulate inside the resonator it is also dissipated by the cavity itself, for this, and for the presence of the external coupling, it is required to maintain the external source active while the system operates, and this feature makes the system a driven-dissipative one, that, as in the recent years has been observed, they are the systems in which new exotic phenomena manifest.

In addition the material responds nonlinearly to the optical field, with the nonlinearity represented, at the first order¹ by the cubic (so called Kerr [13]) nonlinearity, in which the induced polarization density depends cubically on the electric field in the cavity, resulting in an intensity dependence of the refractive index of the material. This nonlinear response couples photons with different frequencies in a nontrivial way, making them interacting through Four-wave mixing processes(FWM) [13]. Since however this nonlinear response acts as a perturbation for the system, it requires high-intensities intracavity optical fields to give a relevant contribution. This is however achieved in the microresonators thanks to the high purity fabrication process, measured by the quality factor Q , that makes the intrinsic optical losses (measured by the parameter κ_0) very small, increasing the photon lifetime enough to enhance the effect of the nonlinearity.

¹Due to the amorphous structure of the Si_3N_4 that make the second order nonlinear response vanishing

Finally, Si_3N_4 is dispersive, meaning that the refractive index depends also on the frequency of the optical mode propagating, due to the microscopic interaction of the electrons of the material and the optical field [13]. This effect leads to a distribution of the resonant frequencies of the resonator along a complex dispersion profile, associating in principle to different optical modes different resonant frequencies.

The interplay of these features gives rise to complex dynamical behaviour of the optical field inside the resonator.

1.1.2 Coupled-mode and Lugiato Lefever equations

Starting from the optical properties of the material, under opportune hypotheses [14], it is possible to derive from Maxwell's equations a dynamical equation for the amplitudes of the resonating modes inside the Kerr microresonators. This has been first done in [14], and the equation is called coupled mode equation and it is here reported:

$$\dot{\mathcal{A}}_\eta = -\frac{1}{2}\Delta\omega_\eta\mathcal{A}_\eta - ig_0 \sum_{\alpha,\beta,\mu} \Lambda_\eta^{\alpha\beta\mu} \mathcal{A}_\alpha \mathcal{A}_\beta^* \mathcal{A}_\mu e^{i\bar{\omega}_{\alpha\beta\mu\eta}t} + \frac{1}{2}\Delta\omega_\eta\mathcal{F}_\eta e^{i(\Omega_0-\omega_\eta)t} \quad (1.1)$$

Where $\bar{\omega}_{\alpha\beta\mu\eta} = \omega_{\alpha} + \omega_{\beta} + \omega_{\mu} - \omega_{\eta}$.

This equation describes the dynamical evolution of the slowly-varying amplitudes ($\{\mathcal{A}_\alpha\}$) of the resonating eigenmodes inside the cavity (whose resonance frequency is ω_α), subjected to its dissipation ($\Delta\omega_\eta$), the cubic nonlinearity (g_0) and the external field (\mathcal{F}_η), oscillating at frequency Ω_0 . The strengths of the coupling between different eigenmodes depends on the overlap of the modes ($\Lambda_\eta^{\alpha\beta\mu}$) and on their differences in frequencies ($\bar{\omega}_{\alpha\beta\mu\eta}$), and it is maximized when they have the same eigenfrequencies, indicating that the nonlinear processes can happen just when particular phase-matching conditions are satisfied

Even if these equations correctly describe the dynamics of the system and give important insights in the actual interactions between different modes, it requires long computational time to simulate it, requiring to numerically solve a big system of coupled equations, since there is no analytical solution known.

After the discovery of the presence in this systems of dissipative solitons [1], it has been found out that the dynamics of the system could be described by an alternative and equivalent [15] equation, known as (1D) Lugiato-Lefever equation(LLE) [16]:

$$\frac{\partial A}{\partial T} = -\left(\frac{\kappa}{2} + i\delta\omega\right)A + i\frac{D_2}{2}\frac{\partial^2 A}{\partial \phi^2} + ig_0|A|^2A + \sqrt{\kappa_{\text{ex}}}\mathcal{S}_{\text{in}} \quad (1.2)$$

This is the equation for A , the complex envelop of the electric field inside the resonator, where in addition to the dissipation (κ), Kerr nonlinearity (g_0) and external

pump (s_{in}), there is the explicit appearance of the dispersion term, represented by the second order derivative and a further dependence on the detuning term $\delta\omega$, defined as:

$$\delta\omega = \omega_0 - \omega_p \quad (1.3)$$

taking in account the difference between the external laser frequency ω_p and the closest cavity resonance ω_0 .

The envelop depends on the so called fast time ϕ that is related to the azimuthal coordinate around the ring², and in fact, due to the ring topology, this field satisfy the periodic boundary conditions, making it possible to be decompose in a discrete series of eigenmodes [15] as follows:

$$A(\phi, T) = \sum_{m \in \mathbb{Z}} \mathcal{A}_m(T) e^{-im\phi} e^{i[\omega_m - (\omega_p + D_1 m)]T} \quad (1.4)$$

Where \mathcal{A}_m are exactly the amplitude described in equation (1.1) The advantages of equation 1.2 is that it describes the dynamics of the field within a single equation in real space, making it faster to numerically solve³.

Equation 1.2 can be further simplified, making the following change of variables⁴:

$$\begin{aligned} t &= \frac{\kappa}{2} T & \theta &= \sqrt{\frac{\kappa}{2D_2}} \phi \\ \zeta_0 &= \frac{2\delta\omega}{\kappa} & \psi &= \sqrt{\frac{2g_0}{\kappa}} A & f &= \sqrt{\frac{8\eta g_0}{\kappa^2}} s_{in} = \sqrt{\frac{P_{in}}{P_{thres} h\omega_0}} \end{aligned} \quad (1.5)$$

and read as follows:

$$\frac{\partial \psi}{\partial t} = - (1 + i\zeta_0) \psi + \frac{i}{2} \partial_\theta^2 \psi + i|\psi|^2 \psi + f \quad (1.6)$$

This formulation of the equation makes evident that the complete description of the physical state of the system is given by the value of the only two parameters ζ_0 and f , and according to the position of the operating point (ζ_0, f) in the two-dimensional space (ζ_0, f) the intracavity field will manifest the presence of Turing rolls [17], chaos [18], rogue waves [18], single and multi-solitons states [1, 2], breathers [19], and stable dissipative solitons. The stability of the different solutions has been studied in dependence on the operating point position through a bifurcation analysis [20] and a Lagrangian approach [21] and the stability map

²To be precise, it is actually defined in a rotating frame inertial to the soliton group velocity such that $\phi = \varphi - D_1 t$, with $\varphi \in [0, 2\pi]$ but it does not change the nature of the consideration

³Look at Chapter 4 for details on the numerical solution algorithm

⁴To note that while in 1.2 the azimuthal coordinate ϕ belongs to $[-\pi, \pi]$, in the normalized version 1.6 θ ranges in $[-\frac{L}{2}, \frac{L}{2}]$ with $L := 2\pi\sqrt{\frac{\kappa}{2D_2}}$, and since $\frac{\kappa}{D_2} \gg 1$, in the following, when integrating along the cavity we will take the limit $L \rightarrow \infty$.

shown in figure 1.3 has been obtained.

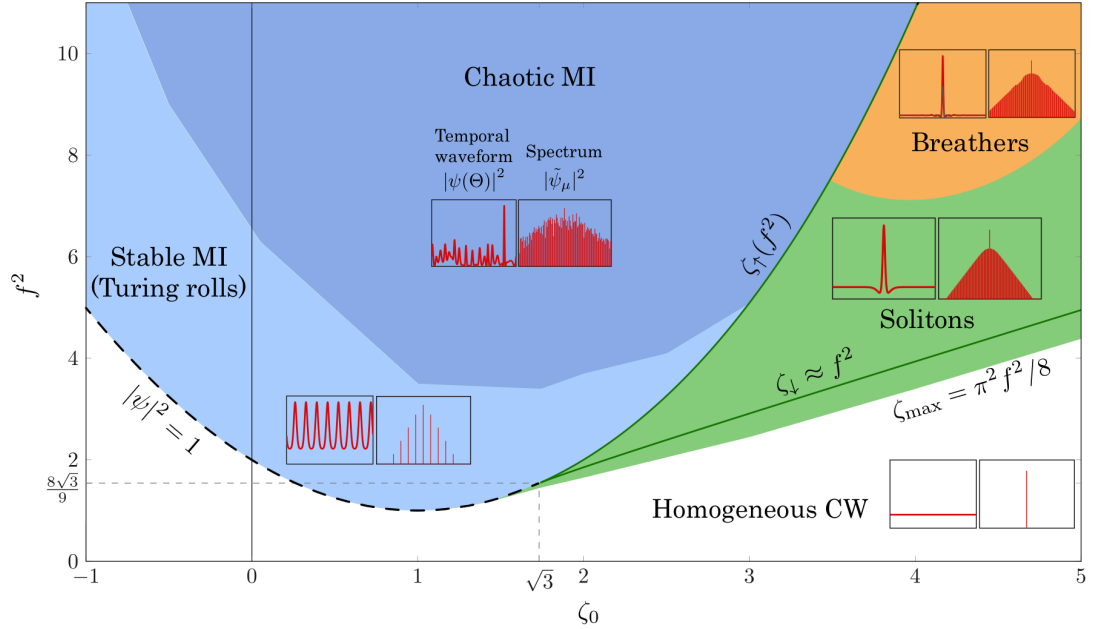


Figure 1.3: Stability Diagram of Lugiato-Lefever equation (figure adapted from [22]). From the figure we can see the stable attractors of the system in dependence of the operating point. With stable MI is intended stable Modulation instability, that is the phenomena by which the homogeneous solution becomes unstable due to four-wave mixing processes, that in an ordered way start occupying more resonating cavity modes, forming the so called Turing rolls, whose spatial profile is visible in the figure. If the detuning ζ_0 is further increased, the system enters in the region of Chaotic MI, where now the resonating modes are occupied in a chaotic way, destabilizing Turing rolls, obtaining a unstructured field distribution inside the resonator. At the end of this region, the breathers or solitons regions are reached, where localized structured becomes stable. See [20] for further details.

1.1.3 Realistic Dispersion Profile and limits of the equation: Higher order Dispersion and Avoided Mode Crossing

The properties and the stability of the soliton state are strongly related to the dispersion profile of the system [23] and it is essential to take them in account. Expressed in this way, equation 1.6 (and consequently 1.2) implies an important assumption, that is the dispersion profile of the optical cavity frequencies is purely

parabolic. This can be seen by rewriting the dispersion term expanding the normalized field in its eigenmodes decomposition Eq. 1.4 [15, 20] as follows⁵:

$$\partial_\theta^2 \psi = \partial_\theta^2 \sum_\mu \psi_\mu(t) e^{i\mu\theta} = - \sum_\mu \mu^2 \psi_\mu(t) e^{i\mu\theta} := - \sum_\mu \hat{D}_{int}(\mu) \psi_\mu(t) e^{i\mu\theta} \quad (1.7)$$

Where we highlighted the presence of the parabolic dispersion defining the dispersion operator \hat{D}_{int} .

Even if this model has been demonstrated to be very precise in predicting the dynamical behaviour of the field in the resonator [24], this parabolic approximation is valid only in the neighborhood of a local minima of the dispersion. Far from that, higher order derivative terms have to be taken in account in the dispersion operator.

More importantly, equations (1.6) assumes that inside the resonator there is only a single family of modes [14], but this assumption is almost never true, since, even for a one dimensional system there is always at least pair of orthogonal modes, i.e. transverse electric (TE) and transverse magnetic (TM) [13].

When two or more mode families coexist inside the resonator, sharing the same mode volume, they interact with an the strength of the interaction depends on the overlap of their optical volumee. This interaction, called avoided mode crossing (AMX) 1.4, prevents the two modes dispersions to be degenerate within the same resonance frequency, leading to an abrupt change of the dispersion profiles in the neighborhood of their interception [25, 26]. This process can be described through the coupled mode equations in the following way [27]:

$$\begin{aligned} \frac{d\mathcal{A}_1}{dt} &= i\omega_1 \mathcal{A}_1 + iJ_{12} \mathcal{A}_2 \\ \frac{d\mathcal{A}_2}{dt} &= i\omega_2 \mathcal{A}_2 + iJ_{21} \mathcal{A}_1. \end{aligned} \quad (1.8)$$

Finding the eigenvalues of the coupling matrix and setting $J_{12} = J_{21} = J$, obtaining:

$$\omega_\pm = \frac{\omega_1 + \omega_2}{2} \pm \sqrt{\left(\frac{\omega_1 - \omega_2}{2}\right)^2 + |J|^2} \quad (1.9)$$

Where we can see, that even in the presence of degeneracy $\omega_1 = \omega_2$, the resulting modes are symmetrically shifted by a contribution proportional to the coupling J, as shown in figure 1.4

While the soliton state has been proven to be robust with respect to the higher order terms of the dispersion profile, the same it is not true for the presence of the mode crossings [23], since it can prevent the soliton formation and induce

⁵We rewrote Eq. 1.4 in its normalized version, incorporating in ψ_μ all the temporal dependence

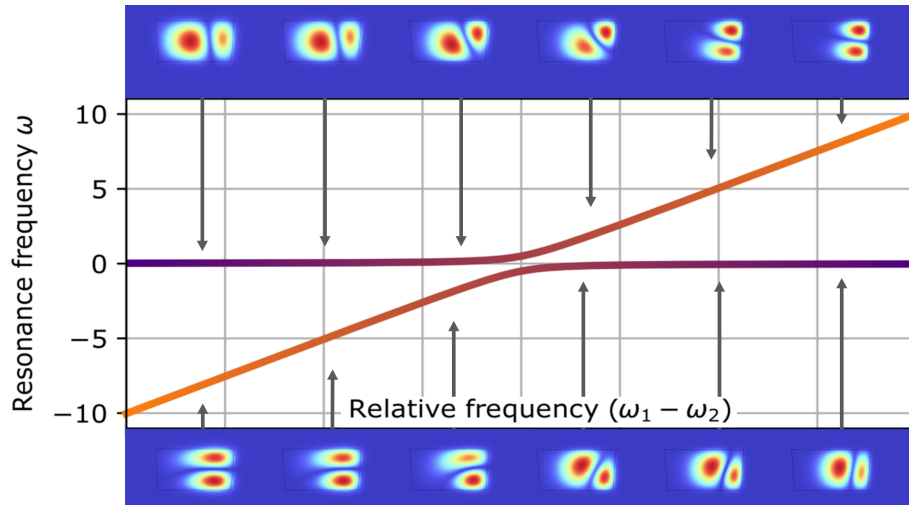


Figure 1.4: Example of Avoided mode crossing interaction. We can see how the dispersions of two modes belonging to different family, interacts avoiding the crossing. Furthermore from the mode profile is possible to see that in the neighborhood of the crossing the two modes hybridize.

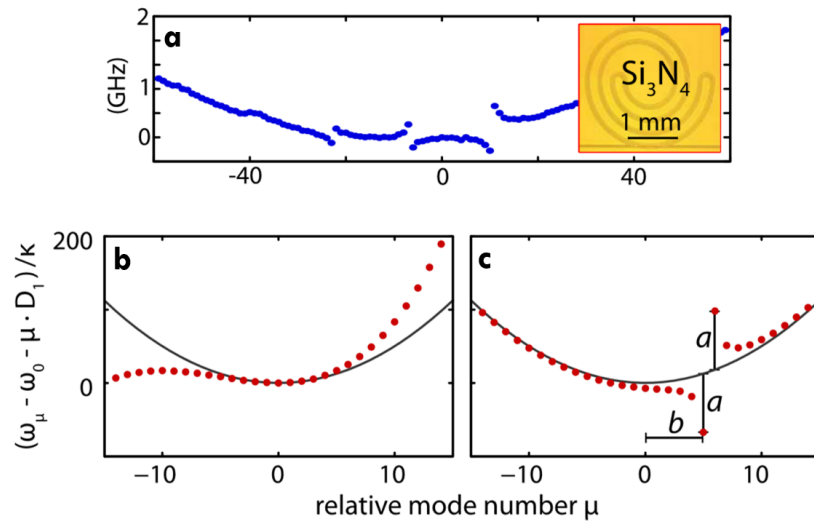


Figure 1.5: Example of a realistic dispersion profile in presence of Avoided mode crossing interaction, figure adapted from [23].

instabilities [28]. Only recently the latter phenomena has been seen also as a potentially useful phenomena, finding out that it can reduce the laser phase-noise

dependence of the soliton dynamics [29], trigger nonlinear dynamics in normal dispersion resonators [30, 31, 32, 33], and control the chaotic state which results in the generation of structured state of light called soliton crystals [34].

In the present work, we focus on deepening the understanding of the phenomena of the noise reduction tightly related to the notion of the quiet point - a particular operating point in the soliton existing range which is characterized by the anomalously low phase noise of the system. We approach this problem via the combination of theoretical and numerical methods applied to a simplified model of the avoided mode crossing, in which only a single mode is shifted from the parabolic dispersion profile. This simple yet efficient model allows us to examine analytically the range of the quiet points existence and confirm it numerically estimating, the resulting phase noise of the generated RF signal.

Chapter 2

Model of the Avoided Mode Crossing

2.1 Perturbed LLE

The model developed in this thesis is a perturbed Lugiato-Lefever equation (LLE) (1.2) in which the resonance of one single resonating cavity mode has been shifted from the pure parabolic dispersion. The perturbation term is obtained starting from equation (1.2) and modifying directly the integrated dispersion operator \hat{D}_{int} as follows:

$$\hat{D}_{int}^{\bar{\mu}}(\mu) = \hat{D}_{int}(\mu) + a_{\bar{\mu}}\delta_{\mu,\bar{\mu}} \quad (2.1)$$

Substituting the following integrated dispersion in the formal definition of LLE (1.2) we obtain:

$$\begin{aligned} \partial_t \psi &= -(1 + i\zeta_0)\psi - i \sum_{\mu} \hat{D}_{int}^{\bar{\mu}}(\mu) \tilde{\psi}_{\mu} + i|\psi|^2\psi + f \\ &\Rightarrow \partial_t \psi = -(1 + i\zeta_0)\psi + \frac{i}{2} \partial_{\theta}^2 \psi + i|\psi|^2\psi + f - ia_{\bar{\mu}} \tilde{\psi}_{\bar{\mu}} e^{i\bar{\mu}\theta} \end{aligned} \quad (2.2)$$

Where now the chosen mode $\bar{\mu}$ has a resonance frequency given by ¹:

$$\omega_{\bar{\mu}} = \frac{\bar{\mu}^2}{2} + a_{\bar{\mu}} \quad (2.3)$$

This is the simplest model deviating from the perfectly parabolic dispersed that can manifest the key feature of the phenomenon of AMX, that of the generation

¹Strictly speaking, it represents the value of its integrated dispersion, but this does not change the following reasoning

of dispersive wave through the interaction of solitonic linear dispersion with the shifted resonance of the $\bar{\mu}$ -th cavity mode of the system [35, 29]. The presence of dispersive wave formation is one of the major characteristic features of the physics of the AMX.

2.2 Properties of the Equation and Conservation Laws

We now study how the perturbation induces changes in the dynamics of two relevant quantity of the system, respectively the norm and the momentum of the field.

2.2.1 Continuity equation for the Norm

From equation 2.2 a dynamical equation for the norm of the intracavity field (i.e. the energy) can be derived. By multiplying eq. (3.9) by ψ^* we obtain:

$$\psi^* \partial_t \psi = -(1 + i\zeta_0)|\psi|^2 + \frac{i}{2}\psi^* \partial_\theta^2 \psi + i|\psi|^4 + f\psi^* - ia_{\bar{\mu}}\tilde{\psi}_\mu e^{i\bar{\mu}\theta}\psi^*, \quad (2.4)$$

where \Re (\Im) is the operator taking the real (imaginary) part of the function to which it is applied. Summing now (2.4) to its complex conjugated, we obtain the following equation for the norm of the field² of the system:

$$\begin{aligned} \psi^* \partial_t \psi + \psi \partial_t \psi^* &\equiv \partial_t |\psi|^2 = \\ &\frac{i}{2}(\psi^* \partial_\theta^2 \psi - \psi \partial_\theta^2 \psi^*) - 2|\psi|^2 + f(\psi + \psi^*) - ia_{\bar{\mu}}(\tilde{\psi}_\mu e^{i\bar{\mu}\theta}\psi^* - \tilde{\psi}_\mu^* e^{-i\bar{\mu}\theta}\psi) \\ &\Rightarrow \partial_t |\psi|^2 + \partial_\theta J_\psi = -2|\psi|^2 + 2f\Re\{\psi\} + 2a_{\bar{\mu}}\Im\{\tilde{\psi}_\mu e^{i\bar{\mu}\theta}\psi^*\} \end{aligned} \quad (2.5)$$

Where with J_ψ we defined the current density associated to the field and is defined as follows:

$$J_\psi = -\frac{i}{2}[\psi^* \partial_\theta \psi - \psi \partial_\theta \psi^*] \quad (2.6)$$

²That it is related to the actual number of photons in the system

If we now integrate equation 2.5 over the ring we obtain:

$$\partial_t \int d\theta |\psi|^2 + J_\psi(\theta)|_{-\frac{L}{2}}^{\frac{L}{2}} = -2 \int d\theta |\psi|^2 + 2f\Re \int d\theta \psi + 2a_{\bar{\mu}}\Im \left\{ \int d\theta \psi_{\bar{\mu}} e^{i\bar{\mu}\theta} \psi^* \right\} \quad (2.7)$$

$$\Rightarrow \partial_t N = -2N + 2f\Re\{\psi_0\} + 2a_{\bar{\mu}}\Im \left\{ \psi_{\bar{\mu}} \int d\theta \psi^* e^{i\bar{\mu}\theta} \right\} \quad (2.8)$$

$$\Rightarrow \partial_t N = -2N + 2f\Re\{\psi_0\} + 2a_{\bar{\mu}}\Im \left\{ |\psi_{\bar{\mu}}|^2 \right\} \quad (2.9)$$

$$\Rightarrow \partial_t N = -2N + 2f\Re\{\psi_0\} \quad (2.10)$$

Where $N := \int d\theta |\psi|^2$ and we used the definition of the Fourier transform both to express the circulation of the field in the pump term and to make appear the modulus squared in the imaginary part.

The integral is taken around the ring so for the periodic boundary condition imposed by the topology the density current is integrated to zero.

Equation (2.10) describes the dynamics of the norm of the field that is strictly related to the actual power in the resonator.

We can see that, as in the case of the unperturbed LLE, the system presents losses and gains indicated respectively by the first and second term of the r.h.s.. More importantly, the derivation shows that the perturbation does not directly contribute to the change of the norm of the system, so that its action has to be considered as a redistribution of the energy around the ring.

Considering the stationary case, that could describe the solitonic case, we obtain:

$$N = f\Re\{\psi_0\} \quad (2.11)$$

Meaning that the condition such that a soliton, or any other stationary wave, can be sustained inside the cavity is that the losses must compensate the gain from the external pump; when this condition are satisfied, additionally, the norm of the field, that is related to the intracavity power, would be proportional to the pump term (i.e. input power) and to the number of photons in the pumped mode.

2.2.2 Dynamics of the Momentum

The second relevant quantity that can be considered in the system is the total momentum of the field defined as:

$$P = \sum_{\mu} \mu |\tilde{\psi}_{\mu}|^2 \quad (2.12)$$

We can further rewrite it in the real space as follows:

$$\begin{aligned}
 P &= \sum_{\mu} \mu |\psi_{\mu}|^2 \\
 &= \frac{1}{2i} \left[\sum_{\mu} (i\mu\psi_{\mu}) \psi_{\mu}^* - \sum_{\mu} (-i\mu_{\mu}^*) \psi_{\mu} \right] \\
 &= \frac{1}{2i} \left[\sum_{\mu} (\partial_{\theta}\psi)_{\mu} \psi_{\mu}^* - \sum_{\mu} (\partial_{\theta}\psi^*)_{\mu} \psi_{\mu} \right] \\
 &= \frac{1}{2i} \int d\theta [\psi^* \partial_{\theta}\psi - \psi \partial_{\theta}\psi^*] \\
 &= \Im \left\{ \int d\theta \psi^* \partial_{\theta}\psi \right\}.
 \end{aligned} \tag{2.13}$$

Taking the time derivative of the equation we obtain:

$$\begin{aligned}
 \partial_t P &= \Im \left\{ \int d\theta \partial_t (\psi^* \partial_{\theta}\psi) \right\} \\
 &= \Im \left\{ \int d\theta (\partial_t \psi^*) \partial_{\theta}\psi \right\} + \Im \left\{ \int d\theta \psi^* \partial_{\theta} \partial_t \psi \right\} \\
 &= \Im \left\{ \left[\psi \partial_t \psi^* \Big|_{-\frac{L}{2}}^{\frac{L}{2}} - \int d\theta \psi \partial_{\theta} \partial_t \psi^* + \int d\theta \psi^* \partial_{\theta} \partial_t \psi \right] \right\} \\
 &= \Im \left\{ 2i \Im \int d\theta \psi^* \partial_{\theta} \partial_t \psi \right\} \\
 &= 2\Im \left\{ \int d\theta \psi^* \partial_{\theta} \partial_t \psi \right\} \\
 &= 2\Im \left\{ \int d\theta \partial_{\theta} \psi^* \partial_t \psi \right\}
 \end{aligned} \tag{2.14}$$

Where, thanks to the periodic boundary conditions, the constant term resulting from the two integration by parts (line 3 and 6) are equal to zero. Considering now the follow formal definition of (2.2):

$$\partial_t \psi = \text{LLE}[\psi] - ia_{\bar{\mu}} \psi_{\bar{\mu}} e^{i\bar{\mu}\theta} \tag{2.15}$$

where with $\text{LLE}[\psi]$ we consider the r.h.s of (1.2), we can write:

$$\begin{aligned}
 \int d\theta \partial_{\theta} \psi^* \partial_t \psi &= \int d\theta \partial_{\theta} \psi^* \text{LLE}[\psi] - ia_{\bar{\mu}} \psi_{\bar{\mu}} \int d\theta \partial_{\theta} \psi^* e^{i\bar{\mu}\theta} \\
 &= \int d\theta \partial_{\theta} \psi^* \text{LLE}[\psi] - ia_{\bar{\mu}} \psi_{\bar{\mu}} \int d\theta \partial_{\theta} \psi^* e^{i\bar{\mu}\theta} \\
 &= \int d\theta \partial_{\theta} \psi^* \text{LLE}[\psi] - ia_{\bar{\mu}} \psi_{\bar{\mu}} \left(- \int d\theta \sum_{\mu} \psi_{\mu}^* i\mu e^{-i\mu\theta} e^{i\bar{\mu}\theta} \right) \\
 &= \int d\theta \partial_{\theta} \psi^* \text{LLE}[\psi] - \bar{\mu} a_{\bar{\mu}} |\psi_{\bar{\mu}}|^2
 \end{aligned} \tag{2.16}$$

Being the term related to the perturbation a real number, equation (2.14) is written as:

$$\partial_t P = 2\Im\left\{\int d\theta \partial_\theta \psi^* LLE[\psi]\right\} \quad (2.17)$$

Obtaining so that the perturbation does not directly alter neither the dynamics of the momentum of the field.

If we now instead assume as a solution a propagating wave of group velocity v i.e.:

$$\psi(\theta, t) = \psi(\theta - v(t)) \Rightarrow \partial_t \psi = -v \partial_\theta \psi \quad (2.18)$$

substituting in equation (2.14) we obtain:

$$\partial_t P = 2\Im\left\{\int d\theta (-v |\partial_\theta \psi|^2)\right\} = 0 \quad (2.19)$$

Considering then that the group velocity of the soliton is related to the ratio [36]:

$$v \propto \frac{P}{N} \quad (2.20)$$

taking in account the previous considerations for the dynamics of the norm, we obtain that a solitonic solution will propagate at constant velocity.

2.2.3 Symmetries of the Equation

We can further obtain some useful information about the symmetry of the equation considering the effective Lagrangian of the system³:

$$\begin{aligned} L &= \int_{\mathcal{R}} d\theta \mathcal{L}(\psi, \psi^*, \theta) \\ &= \int_{\mathcal{R}} d\theta \left[\frac{i}{2} (\psi^* \partial_t \psi - \psi \partial_t \psi^*) - \frac{1}{2} |\partial_\theta \psi|^2 + \frac{|\psi|^4}{2} - \zeta_0 |\psi|^2 - i |\psi|^2 + i f(\psi + \psi^*) \right] \\ &\quad - a_{\bar{\mu}} |\psi_{\bar{\mu}}|^2 \\ &= \int_{\mathcal{R}} d\theta \left[\frac{i}{2} (\psi^* \partial_t \psi - \psi \partial_t \psi^*) - \frac{1}{2} |\partial_\theta \psi|^2 + \frac{|\psi|^4}{2} - \zeta_0 |\psi|^2 \right] \\ &\quad - a_{\bar{\mu}} \int_{\mathcal{R}, \mathcal{R}} d\theta d\theta' \psi(\theta') e^{i\bar{\mu}(\theta - \theta')} \psi^*(\theta) \end{aligned} \quad (2.21)$$

Where the integral are taken around the ring. We can see at first that the Lagrangian density dependence of the position comes just from the perturbation term (last

³We are considering in the Lagrangian also the nonconservative terms. It can be easily verified that $\frac{\delta L}{\delta \psi^*} = 0$ is equivalent to (2.2)

term).

Rewriting the Lagrangian density as follows:

$$\mathcal{L} = \mathcal{L}_0(\psi, \psi^*) + \delta\mathcal{L}(\psi, \psi^*, \theta) \quad (2.22)$$

$$\delta\mathcal{L}(\psi, \psi^*, \theta; \bar{\mu}, a_{\bar{\mu}}) := -a_{\bar{\mu}} \int_{\mathcal{R}} d\theta' \psi(\theta') e^{i\bar{\mu}(\theta-\theta')} \psi^*(\theta) \quad (2.23)$$

we firstly concentrate on the properties of $L_0 := \int d\theta \mathcal{L}_0$.

We note that due to the periodic boundary condition and from the absence of explicit dependence of \mathcal{L}_0 on the spatial coordinate it follows that the unperturbed Lagrangian is symmetrical under any space translation so that:

$$\theta \rightarrow \theta' = \theta + c \quad (2.24)$$

Furthermore, from the following relations:

$$\int_{-L/2}^{L/2} d\theta F[\phi(\theta), \partial_t \phi(\theta)] = - \int_{L/2}^{-L/2} d\theta F[\phi(-\theta), \partial_t \phi(-\theta)] = \int_{-L/2}^{L/2} d\theta F[\hat{P}\phi, \partial_t \hat{P}\phi] \quad (2.25)$$

$$|\partial_\theta \psi(-\theta)|^2 = |-\partial_\theta \psi(-\theta)|^2 = |\partial_\theta \hat{P}\psi|^2 \quad (2.26)$$

we obtain that the unperturbed Lagrangian is invariant under the parity transformation of the field:

$$\psi \rightarrow \psi' = \hat{P}\psi \quad (2.27)$$

where \hat{P} is defined as:

$$\hat{P}\psi = \psi(-\theta) \quad (2.28)$$

This symmetry could be deduced from the symmetry of the parabolic dispersion (i.e. distribution of modes) and it is equivalent to the following transformation in Fourier space:

$$\mu \rightarrow -\mu \quad (2.29)$$

Where each mode is replaced to its opposite counterpart. These are the symmetries found in the unperturbed system.

Moving now to the perturbation term $\delta\mathcal{L}$, we can see that it presents different properties depending on the value of μ and in particular in the cases $\bar{\mu} = 0$ and $\bar{\mu} \neq 0$, that we analyze separately in the following.

2.2.4 Case $\mu = 0$

In this case $\delta\mathcal{L}$ loses its spatial dependence (the dispersion in this case, even if not perfectly parabolic, it is still symmetric) and the perturbation of the Lagrangian is

written as:

$$-a_{\bar{\mu}} \int d\theta d\theta' \psi(\theta') e^{i\bar{\mu}(\theta-\theta')} \psi^*(\theta) \xrightarrow{\bar{\mu}=0} -a_0 \left| \int d\theta \psi(\theta) \right|^2 = -a_0 |\tilde{\psi}_0|^2 \quad (2.30)$$

So the Lagrangian is perturbed with a term depending on the modulus squared of the circulation of the field, term that preserves both the translational invariance (due to the ring geometry), the parity ($\psi(\theta) \rightarrow \psi(-\theta)$) and the inversion ($\mu \rightarrow -\mu$) symmetries of the unperturbed Lagrangian.

2.2.5 Case $\mu \neq 0$

Differently, in the case $\bar{\mu} \neq 0$, the perturbation $\delta\mathcal{L}$ introduces now an explicit spatial dependent term in the Lagrangian density \mathcal{L} .

However this dependence is periodic, being represented by a plane wave, of period $\frac{2\pi}{\bar{\mu}}$.

This results in the following invariance of the Lagrangian density ⁴:

$$\delta\mathcal{L}(\theta + \alpha) = \delta\mathcal{L}(\theta) \quad (2.31)$$

for $\alpha = \frac{2\pi n}{\bar{\mu}}$ leading to the discrete translational symmetry under the transformation:

$$\theta \rightarrow \theta' = \theta + \alpha \quad (2.32)$$

Reminding that the periodic boundary conditions of the systems imposes for any resonant mode numbers to be as⁵⁶:

$$\mu = \frac{2\pi m}{L} \quad (2.33)$$

Where L is the length of the cavity, we can rewrite the period as:

$$\alpha = \frac{2\pi}{\bar{\mu}} = \frac{2\pi L}{2\pi \bar{m}} = \frac{L}{\bar{m}} \quad (2.34)$$

This symmetry could already be seen from (2.2) Furthermore, from the explicit dependence of $\delta\mathcal{L}$ also on the particular mode $\bar{\mu}$, we can see that, as expected

⁴We remind that \mathcal{L}_0 is already invariant under any spatial translation

⁵Refer to equation (1.4)

⁶Due the relation 2.33, we can uniquely refer to any mode number μ by referring to its relative integer counterpart m . We will do so and in the following, whenever we will refer to an integer mode displaced, i.e. $\bar{\mu} = \bar{m}$ we will be referring to $\bar{\mu} = \frac{2\pi}{L}\bar{m}$

by the asymmetric dispersion profile, it is not invariant under the transformation $\mu \rightarrow -\mu$ in fact:

$$a_{\bar{\mu}} \int_{-L}^L d\theta \int_{-L}^L d\theta' \psi(\theta') e^{i\bar{\mu}(\theta-\theta')} \psi^*(\theta') \xrightarrow{\mu \rightarrow -\mu} a_{\bar{\mu}} \int_{-L}^L d\theta \int_{-L}^L d\theta' \psi(\theta') e^{-i\bar{\mu}(\theta-\theta')} \psi^*(\theta') \quad (2.35)$$

Moreover, if we further develop the r.h.s of (2.35) we obtain:

$$\begin{aligned} & a_{\bar{\mu}} \int_{-L}^L d\theta \int_{-L}^L d\theta' \psi(\theta') e^{-i\bar{\mu}(\theta-\theta')} \psi^*(\theta') \\ &= a_{\bar{\mu}} \int_{-L}^L d(-\theta) \int_{-L}^L d(-\theta') \psi(-(-\theta')) e^{i\bar{\mu}((-\theta)-(-\theta'))} \psi^*(-(-\theta)) \\ &= a_{\bar{\mu}} \int_{-L}^L dx \int_{-L}^L dx' \psi(-x') e^{i\bar{\mu}(x-x')} \psi^*(-x) \\ &= a_{\bar{\mu}} \int_{-L}^L dx \int_{-L}^L dx' \hat{P} \psi(x') e^{i\bar{\mu}(x-x')} \hat{P} \psi^*(x) \end{aligned} \quad (2.36)$$

The system, after the inversion $\mu \rightarrow -\mu$ in fact, even if behaves differently, it has the exact same dynamics of the field $\hat{P} \psi$, so that the perturbed system results symmetric with respect to a more general symmetry $P - \mu$ -symmetry.

2.3 Simulations

2.3.1 Dimensionality of parameter space and choice of the pump power

As it has been seen in chapter 1, the dynamical behaviour of the system described by the pure LLE is defined by a point (so called operating point) in the two-dimensional parameters space spanned by the pump f and detuning ζ_0 parameters, the only two parameters on which \mathcal{L}_0 depends on. The perturbation $\delta\mathcal{L}$ introduces two further parameters in the model, resulting in an increase of the dimensionality of the parameters space, becoming 4-dimensional, since in principle the resonance shift $a_{\bar{\mu}}$ and the displaced mode number $\bar{\mu}$ are independent.

In order to simplify the study of the dynamical properties of the system we operate in a three-dimensional subspace $(\zeta_0, a_{\bar{\mu}}, \bar{\mu})$, fixing the value of the pump term to $f = \sqrt{6}$ to maintain the system far from the region of transient and spatiotemporal chaos described in [37], thus being able to stably access the solitonic states.

2.3.2 Case $\bar{\mu} = 0$

In this case, the dispersion profile of the system is still symmetric even if not exactly parabolic due to the displaced pump mode. However, given the fact that

the inversion symmetry ($\mu \rightarrow -\mu$) is still preserved, the only constant momentum⁷ the system can have is zero momentum.

Furthermore, as highlighted in the supplementary informations of [38], in the stationary state, the presence of the perturbation becomes equivalent to rescaling and phase shifting of the pump term⁸. Thus in this case, the soliton solution is exactly equivalent to the dissipative Kerr soliton of the LLE.

It has been demonstrated, that the phase shift of the pump can facilitate the soliton generation [38] and increase pump-to-soliton conversion efficiency, as demonstrated in [39]. This occurs due to the change in the properties of the bifurcation diagram, making different attractors stables in different operating points of the parameters space of the system.

We have observed these results from the simulated dynamics depicted in figure 2.1. The beginning of the modulation instability region depends strongly on the strengths of the displacement, justified from the fact the in this way we practically change the frequency of the pump, effectively exciting the system already in a red or blue-side detuning regime. In this way, the system can start the dynamics directly in the soliton existence range, chaotic or stable MI.

Since this case has been already studied in Refs. [38, 39], we will not focus on this case during the rest of the work, however we reported this results for completeness.

2.3.3 Case $\bar{\mu} \neq 0$

As discussed in the previous section, the system demonstrates an explicit asymmetry in the dispersion profile. This results into the acquisition of the soliton of a constant momentum different from zero as can be seen in figure 2.2. Still from 2.2 it is possible to see that the soliton and the background are in phase, propagating together at the same speed and in the same direction.

In addition, as we can see from the soliton profile in figure 2.3, there it manifests a periodic modulation of the background (referred as dispersive wave) superimposed to the soliton, characterized by the exact period imposed by the perturbation term $\delta\mathcal{L}$ described in 2.6.

That has been justified by the fact that the asymmetry in the distribution of modes imposed by the perturbation induces a surplus or a deficit in the number of photons in the displaced mode, i.e. $|\psi_{\bar{\mu}}|^2$ with respect to the unperturbed value. In fact, while in the unperturbed case the contribution of the different modes perfectly

⁷See (2.14)

⁸We remind that in LLE the pump term can be assumed real with the condition that all the phase of the system are defined relative to the actual pump phase[15], and here the same can be done in the stationary case

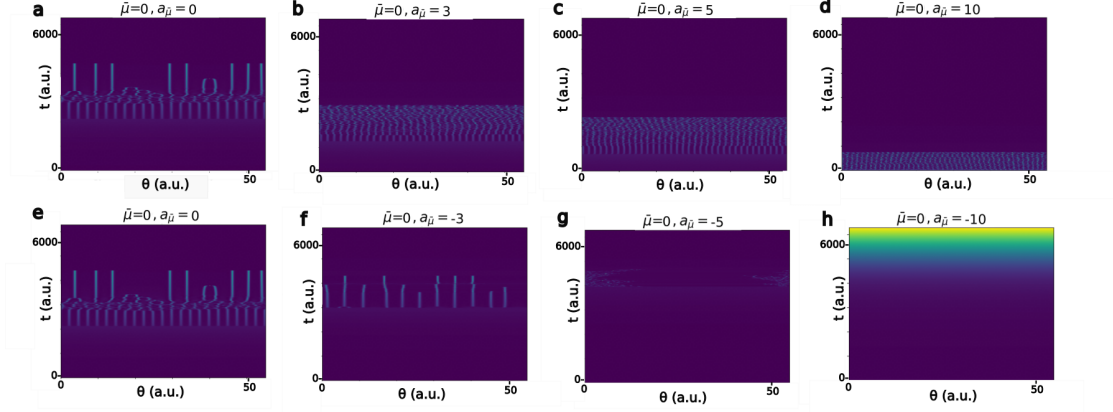


Figure 2.1: Tuning to resonance for different resonance shift $\bar{\mu} = 0$. a) No resonance shift, b) $a_{\bar{\mu}} = 3$, c) $a_{\bar{\mu}} = 5$, d) $a_{\bar{\mu}} = 10$. e) No resonance shift, f) $a_{\bar{\mu}} = -3$, g) $a_{\bar{\mu}} = -5$, h) $a_{\bar{\mu}} = -10$. We can see that according to the strength of the resonance shift the system is found in a different region of the parameter space, as already verified in [39]

superimpose (1.4), compensating each other, resulting in a flat soliton background, in the presence of the shifted resonance, only the shifted mode $\bar{\mu}$ contribution to the superposition will be different, and the exceeding (or lacking) contribution will result in the periodic tail. In formulas:

$$\psi^{Soliton}(\theta, t) = \sum_{\mu} \psi_{\mu}^{Soliton}(t) e^{i\mu\theta} \quad (2.37)$$

$$\psi^{AMX}(\theta, t) = \sum_{\mu \neq \bar{\mu}} \psi_{\mu}^{Soliton}(t) e^{i\mu\theta} + (\psi_{\bar{\mu}}^{Soliton} + \delta\psi_{\bar{\mu}}) e^{i\bar{\mu}\theta} = \psi^{Soliton}(\theta, t) + \delta\psi_{\bar{\mu}} e^{i\bar{\mu}\theta} \quad (2.38)$$

Where $\psi^{Soliton}$ indicates the DKS of LLE with flat background and ψ^{AMX} the soliton solution within the following model. This explains also the variation in the amplitude observed for different frequency shift $a_{\bar{\mu}}$. As we can see in 2.4 in fact, the amplitude (and so the occupancy $|\psi_{\bar{\mu}}|^2$) depends on the frequency shift, and this, as explained in [40, 35], is due to the dependence of the phase matching conditions between the soliton dispersion and the displaced resonance, that changes if the resonance is shifted.

As already observed, the dispersive wave is phase-locked to the soliton. This is a key properties, since in this way the presence of the dispersive wave increases the interaction range of the soliton, that becomes now more correlated to the entire cavity.

This results in the stabilization of multisolitons states, as discussed in [41], allowing

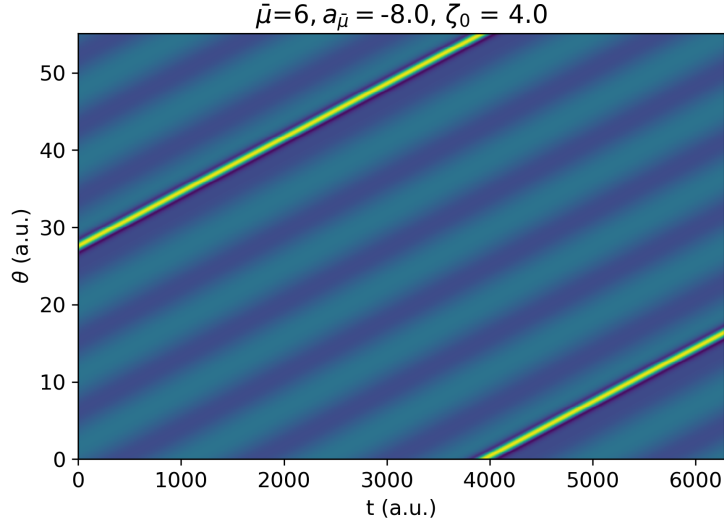


Figure 2.2: Single soliton simulated dynamics. We can see the simulated soliton (light green line) propagating along the azimuthal coordinate θ during time t for the operating point $(\zeta_0, a_{\bar{\mu}}, \bar{\mu}) = (4, -8, 6)$. Both the modulation of the background and the presence of periodic boundary conditions are visible.

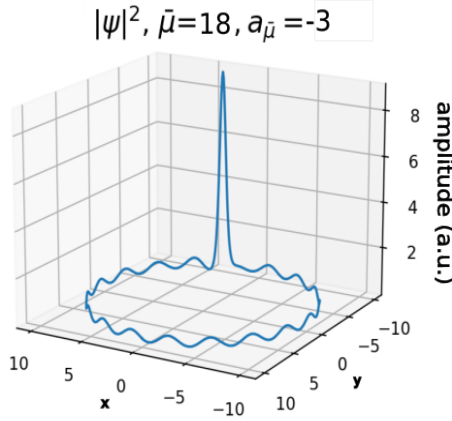


Figure 2.3: Dissipative cavity soliton. Simulated soliton for $\bar{\mu} = 18$. As already demonstrated, the period is related to the mode number, such that there are exactly 18 "hills" in the dispersive tail of the soliton.

the solitons to propagate closer to each other without interacting and subsequently annihilating, as normal in the LLE dynamics. This property manifests, in the extreme case, as the existence of a new multisoliton state, the so called Soliton crystal which presents a radially symmetrical distribution of solitons around the

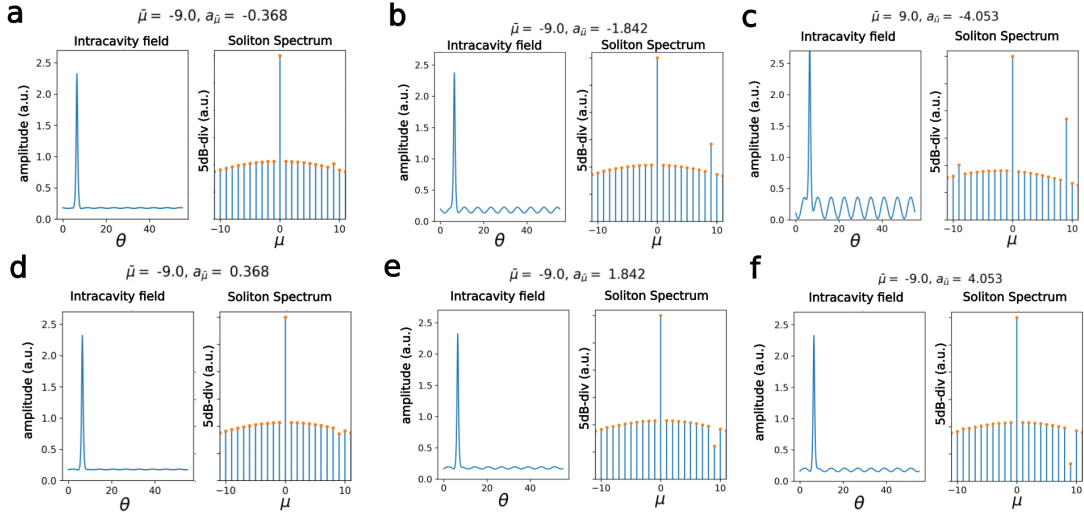


Figure 2.4: Solitons in real space and their spectra for different resonance shifts $a_{\bar{\mu}}$.

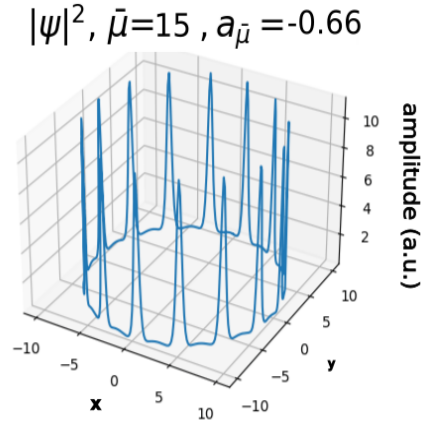


Figure 2.5: Soliton Crystal state. Soliton crystal state, ($a_{\bar{\mu}} = -0.66, \bar{\mu} = 15$). We can see how the period (i.e. lattice length) is exactly equal to the number of mode displaced, this due to the presence of the modulated background.

ring, which, as observed in [37], is instead an unstable solution for the unperturbed LLE. In addition, the number of solitons forming the crystal is exactly equal to the mode number of the mode displaced, highlighting again the importance of the dispersive wave for the crystallization process.

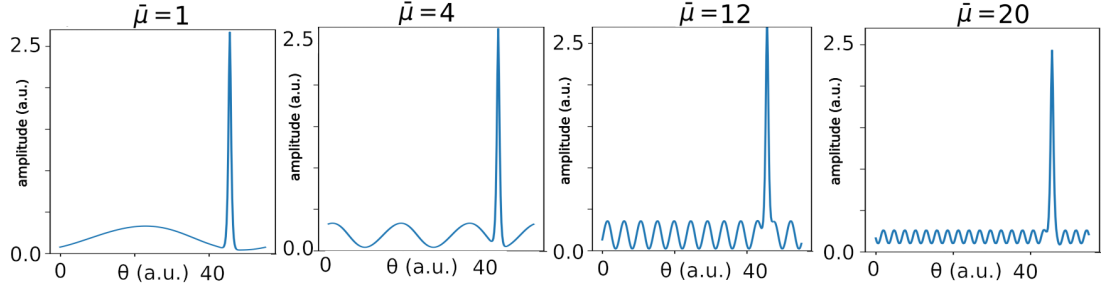


Figure 2.6: Periodicity of the soliton background Different stable soliton solution for different mode number $\bar{\mu}$ displaced.

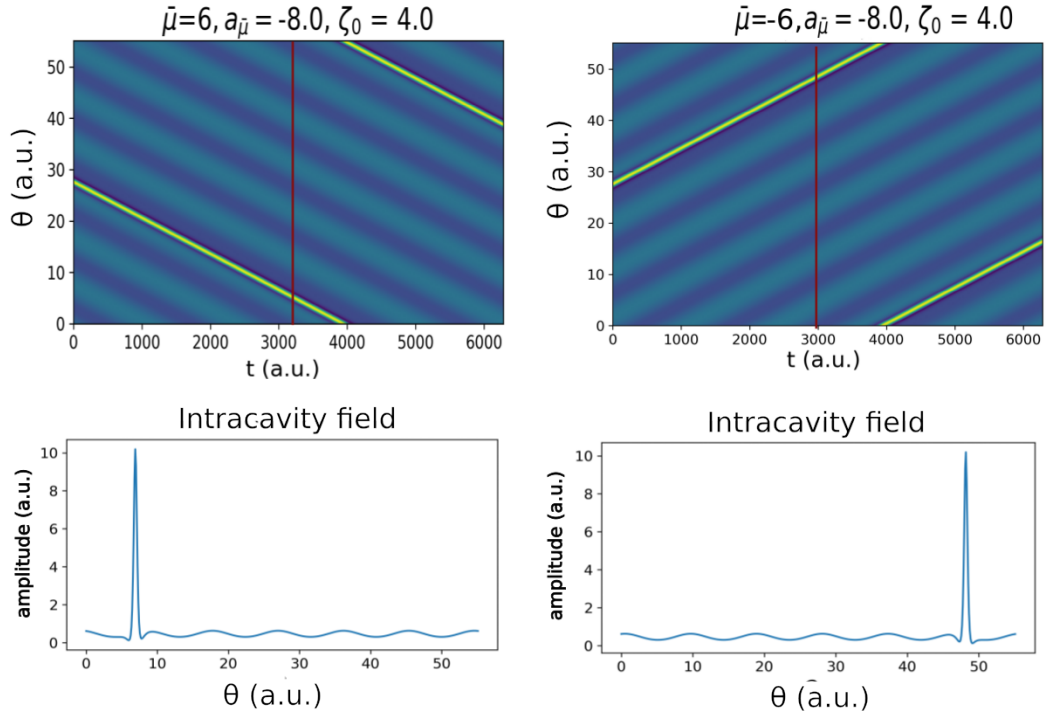


Figure 2.7: $P-\mu$ Symmetry We can clearly see from the figures how the dynamics for two operating points in the parameters (sub)space $(\zeta_0, a_{\bar{\mu}}, \bar{\mu})$ -plane, differing only for the value of $\bar{\mu}$, equal to $\bar{\mu} = 6$ (left) and $\bar{\mu} = -6$ (right), is related by a parity transformation.

Chapter 3

Noise reduction and Microwave generation

Among the numerous applications of Kerr microresonators, the microwave generations is often considered as a primary one. Without entering the details of the engineering of an actual device and the implications such devices, we will give here a simple conceptual description of the phenomena.

In the ideal case, a dissipative soliton obeying the Lugiato Lefever equation, at fixed detuning and pump power, will circulate in the ring at a constant group velocity.

Due to the coupling between the waveguide and the cavity 1.2, part of the intracavity field is dissipated, being outcoupled.

If we then place a photodiode at the output port of the integrated circuit, it will detect a train of identical optical pulses equally separated in time, by a constant time interval, τ_R called the roundtrip time, since it is the time in which the soliton make a complete round around of the cavity. Being the latter of the order of microseconds, the optical signal will be converted to the microwave domain with constant frequency f_R . This frequency is called repetition rate and it is related to the roundtrip time by the following relation:

$$f_{rep} = \frac{1}{\tau_R} \quad (3.1)$$

In this ideal case a perfect microwave generator could be realized.

In a real world situation instead, the process of creating a trustful integrated radio-frequency signal generator is hindered by the presence of different noise sources in the system. Some of them are intrinsic to the resonator, due to the coupling of photonic intracavity field to the phononic degrees of freedom of the

cavity; since the latter depend on the temperature field within the resonator, the result is an effective coupling of the intracavity optical and the temperature fields, known as thermo-optic effect. This can be modeled as a further temperature dependence of the refractive index of the system and leads, to the coupling of fluctuations of the temperature field to the fluctuations of the cavity resonances, giving rise to the major thermal noise contribution, known as thermo-refractive noise, firstly experimentally characterized in Silicon nitride resonators in [42]. The second main sources of noise are instead related to the nature of the external driver. One of that is the shot noise, a fundamental noise source arising from the discrete nature of the electromagnetic field produced by the driver that leads to a fluctuating number of photons emitted in time.

Finally, the driver field, far from being ideal, fluctuates both in phase and amplitude, leading to two further independent sources of noise that affects the soliton dynamics [40].

The presence of these stochastic effects results in a fluctuation of the soliton group velocity, that will lead to a fluctuation of the roundtrip time and consequently to a fluctuating repetition rate of the microwave generator. In particular, as underlined in [43], the major contributors to the soliton noisy dynamics are the thermo-refractive noise and the phase noise of the laser. For this, in the work we focused explicitly on the presence of pump phase noise, showing how the presence of a single shifted resonance, if opportunely engineered, can compensate the presence of the noise, stabilizing the soliton dynamics.

3.1 Noise transduction mechanism

The response of the resonator to the presence of the noise depends strongly on the material. For instance if the material is ideally parabolic dispersed, so exactly described by the Lugiato Lefever equation, it would be insensitive to external phase noise of the laser [40],¹ being the group velocity independent on the detuning. In a real system instead the dispersion profile is more complex than simple parabolic, presenting higher orders of dispersion and multiple mode families interacting (earlier presented AMX); this leads to the generation of dispersive waves due to the resonant (phase-matched) interaction between the soliton linear dispersion and one or more resonance frequency of the cavity. Being the strength of the soliton-dispersive wave interaction detuning dependent, this makes the soliton susceptible of the frequency noise of the laser.

¹Assuming the system is evolving in the (ζ_0, f) parameter space far from the soliton existence range, otherwise, the noise could move the system to another attractor different from the soliton one

Furthermore, the presence of a further coupling of the intracavity optical field to the vibrational degrees of freedom of the cavity can give rise to the so called Raman scattering², an interaction that breaks the inversion symmetry and allows the soliton to acquire a defined detuning dependent group velocity [44].

Recent studies [29, 45] have shown that the combined action of both these phenomena could surprisingly results in a noise reduction of the system, reaching the so called quiet point (QP), an operating point in the parameter space characterised by the lowest sensitiveness to noise of the system. We extended the perturbed model presented in chapter 2 to take in account both the pump noise and the Raman interaction to show how already the presence of a very narrow and localized AMX (i.e. single resonance shift) could be sufficient to induce a noise reduction.

3.2 Extension of the model: Detuning Noise

In order to take in account the presence of pump phase noise, we followed exactly the same calculation proposed in [14], with the only extension of introducing a further time dependent phase to the input field, obtaining the following noise-dependent version of the coupled mode equation 1.1³:

$$\begin{aligned} \dot{\mathcal{A}}_\mu = & -\frac{\Delta\omega_\mu}{2}\mathcal{A}_\mu - ig_0 \sum_{\alpha\beta\gamma} \Lambda_\mu^{\alpha\beta\gamma} \mathcal{A}_\alpha \mathcal{A}_\beta^* \mathcal{A}_\gamma e^{i\bar{\omega}_{\alpha\beta\gamma}t} \\ & + \frac{1}{2}\Delta\omega_\mu F_\mu \sqrt{1 + \delta\rho^2} e^{i(\Omega_0 t + \varphi(t) + \delta\phi(t) - \omega_\mu t)} \end{aligned} \quad (3.2)$$

Making the following change of variable:

$$\mathcal{B}_\mu = \mathcal{A}_\mu e^{-i(\Omega_0 t + \varphi(t) + \delta\phi(t) - \omega_\mu t)} \quad (3.3)$$

we obtain the following equation:

$$\dot{\mathcal{B}}_\mu = -\left(\frac{\Delta\omega_\mu}{2} + i(\Omega_0 + \dot{\varphi} + \dot{\delta\phi} - \omega_\mu)\right)\mathcal{B}_\mu - ig_0 \sum_{\alpha\beta\gamma} (\Lambda')_\mu^{\alpha\beta\gamma} \mathcal{B}_\alpha \mathcal{B}_\beta^* \mathcal{B}_\gamma \quad (3.4)$$

$$+ \frac{1}{2}\Delta\omega_\mu F_\mu \sqrt{1 + \delta\rho^2} \quad (3.5)$$

²In Si_3N_4 microresonators the effect of Raman scattering is experienced but not for the silicon nitride cavity itself, having a small Raman coupling constant, but due to the stronger coupling of the Silica (SiO_2) substrate over which the integrated circuit is grown

³See Ref. [15] for the equivalence between the two version of the equation

with:

$$\delta\rho^2 := \frac{\dot{\varphi}^4 + 4\dot{\varphi}^2\Omega_0^2 + 4\dot{\varphi}^3\Omega_0 + \ddot{\varphi}^2}{\Omega_0^4} \quad (3.6)$$

$$\delta\phi(t) := \tan^{-1}\left(\frac{\ddot{\phi}}{\Omega_0^2 + \dot{\varphi}^2 + 2\dot{\varphi}\Omega_0}\right) \quad (3.7)$$

$$\Lambda' := \Lambda e^{-i(\Omega_0 t + \varphi(t) + \delta\phi - \omega_\mu t)} \quad (3.8)$$

The introduction of a phase noise in the driver field translates so in a duplex contribution to the dynamics. A first term that is responsible for a time fluctuation of the detuning term and a second one responsible both for the amplitude noise of the pump term. Considering the noise terms as perturbations, we decided to work in the simplified assumptions of assuming, as leading term responsible for the noisy dynamics, the detuning noise term.

Doing so we assumed the following dynamical equation⁴:

$$\partial_t\psi = -(1 + i(\zeta_0 + \delta\zeta(t)))\psi + \frac{i}{2}\partial_\theta^2\psi + i|\psi|^2\psi + f - ia_{\bar{\mu}}\tilde{\psi}_{\bar{\mu}}e^{i\bar{\mu}\theta} \quad (3.9)$$

Where the phase noise of the pump is taken in account through a time dependent detuning term, distributed according to the frequency noise power spectral density of the driving laser.

3.2.1 Simulated Soliton Dynamics in Presence of Noise

Implementing the algorithm described in Chapter 4, we numerically solved equation (3.9) to see the response of the system in presence of the noise⁵.

In all the simulation in this section the soliton seems fluctuating around a preferred position in the ring but this is an artifact due to compensation in the simulation of the mean group velocity of the soliton, so that we can analyze only the noisy dynamics. In the actual simulation the soliton will propagate around the ring linearly with time with a constant group velocity that fluctuates around a constant mean value.

We first simulated the detuning term as a deterministic sinusoidal function of time (cf. Fig. 3.1a) obtaining the results shown in figure 3.1. From Fig. 3.1b we can

⁴Refer to Ref. [15] for the details on the equivalence between equations (3.5) and (3.9)

⁵Due to the $P - \mu$ -symmetry of the model, that is detuning independent, in this section we simulated the dynamics just for positive mode displaced, i.e. $\bar{\mu} > 0$. Furthermore, since we are interested in the case in which there is greatest contribution due to the perturbation, we chose to work with $a_{\bar{\mu}} < 0$, such that there is greatest interaction between soliton and displaced mode.

clearly see that the soliton group velocity depends directly on the detuning value, following with its trajectory exactly the detuning changes. This can be justified by looking at the dynamics in the Fourier space⁶ (cf. Fig. 3.1c); we can see in fact how the linear dispersion of the soliton rotate coherently according to the detuning, going from a region of coherence of signs between the frequencies and the mode numbers, leading to a backward propagation of the soliton, to regions in which the frequencies have opposite signs with respect to the mode numbers, resulting to forward propagation of the soliton. In addition, it can be seen that, the shifted mode $\bar{\mu}$ is majorly occupied with respect to the other modes, justifying the presence of the dispersive wave during the whole dynamics. That shows that the soliton and the dispersive wave are behaving as an unique global structure and not as two independent entities(3.1 a and d).

⁶InFig. 3.1c, as in the following other, we analyzed the dynamics also in the Fourier space, by taking the 2D-Fourier transform of the real space soliton dynamics; in this way it is possible to observe the linear dispersion of the soliton

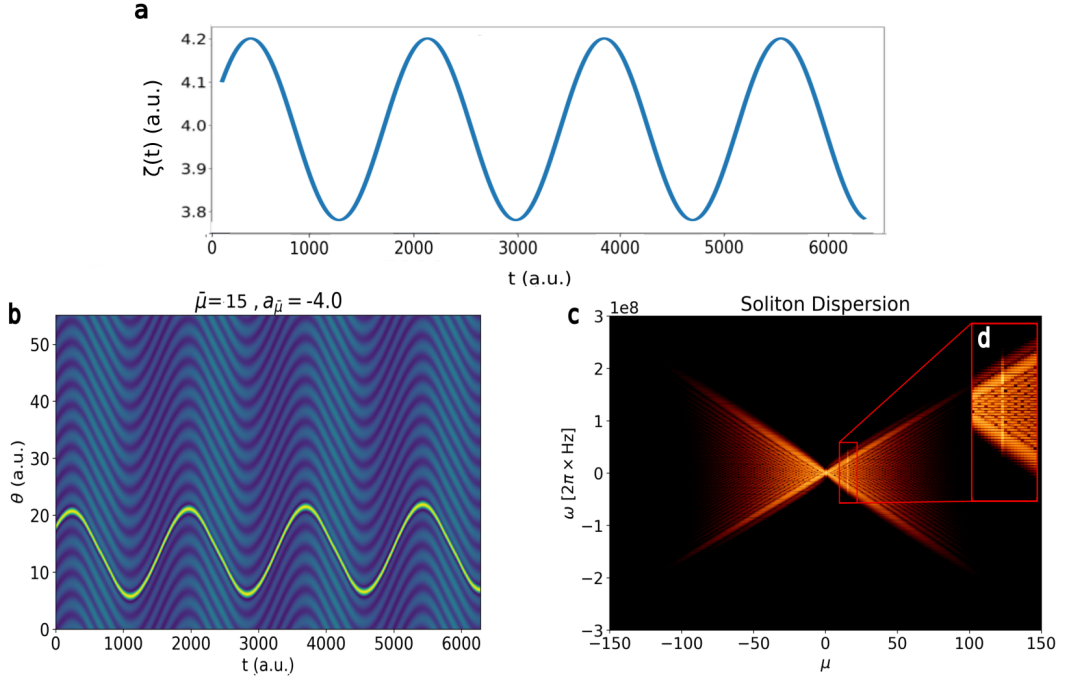


Figure 3.1: Simulated soliton dynamics in presence of sinusoidal modulation of the detuning. $\bar{m} = 15$, $f^2 = 6$, $\zeta_0 = 4$, $\delta\zeta(t) = 0.1\zeta_0 \cos(at + \varphi)$, $\alpha = 0.0033$, $\varphi = -200$. a) Detuning b) (log scale) Real space soliton dynamics: we can see that the soliton and the dispersive wave are phase locked, responding coherently to the noise. c) Response of the soliton in Fourier space: The linear dispersion of the soliton change angle periodically, following the detuning change. d) Zoom of the linear dispersion: we can see how the presence of the modulated background for different detuning shows that at any detuning the soliton dispersion is phase matched with the displaced resonance of mode $\bar{\mu}$.

We further simulated the dynamics in presence of a purely random noise with Lorentian distribution (cf. Fig. 3.2). We can see the soliton state is still preserved also with a fast changing detuning dynamics such as that of a stochastic noise, showing that it is a robust coherent structure with respect to detuning. Furthermore, the same consideration as in the previous case of sinusoidal noise can be done, such that the dispersive wave is still phase-locked to the soliton. Thanks to the previous simulation, now it is easier to understand from Fig. 3.2c, as the linear dispersion of the soliton randomly changing slope with in response of the random detuning.

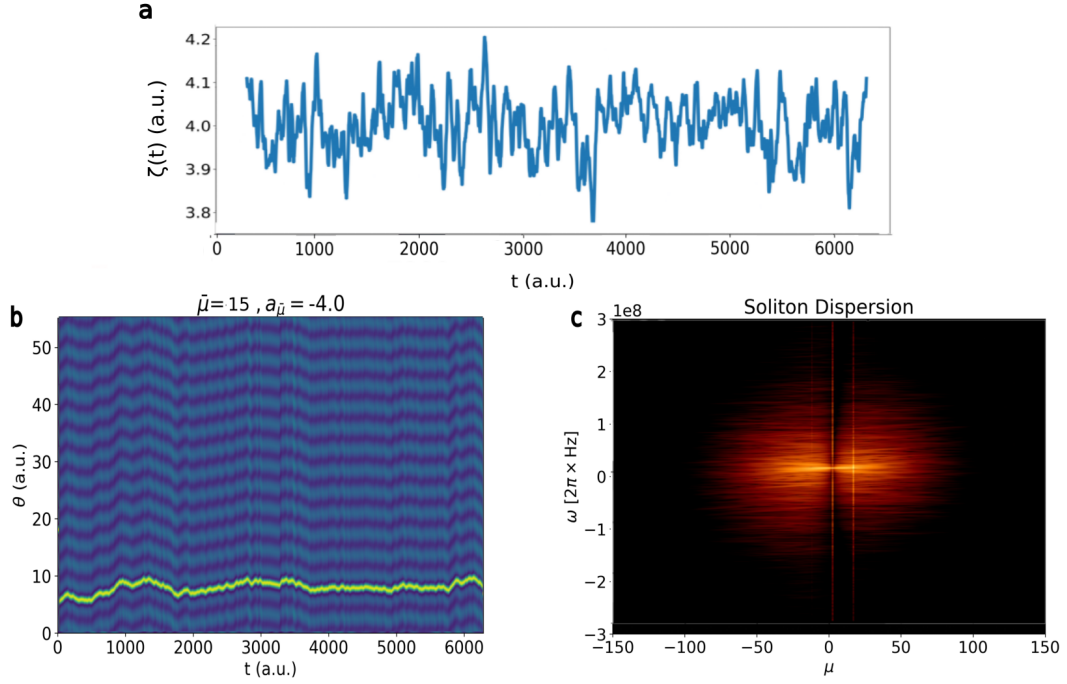


Figure 3.2: Simulated soliton dynamics in presence of random noise and single mode displaced only. $\bar{m} = 15$, $f^2 = 6$, $\zeta_0 = 4$ a) Stochastic Detuning b) (log scale) Real space soliton dynamics c) Response of the soliton in Fourier space

3.3 Extension of the model: Raman Scattering

As previously explained, Raman scattering is due to the interaction between the intracavity field and the vibrational degrees of freedom of the Silica substrate over which the photonic circuit is fabricated. Its contribution to the LLE has already been derived starting from Maxwell wave equation [46], adding a further term to the nonlinear susceptibility of the system, representing the retarded response of the system due to the material vibrational degree of freedom⁷. In addition, following the approach carried on in Ref. [44], only the first order of the Raman response has been taken in account. In this way the the following equation is obtained:

$$\partial_t \psi = -(1 + i(\zeta_0 + \delta\zeta(t)))\psi + \frac{i}{2}\partial_\theta^2 \psi + i|\psi|^2 \psi + f - ia_{\bar{\mu}} \tilde{\psi}_{\bar{\mu}} e^{i\bar{\mu}\theta} - i\tau(\partial_\theta |\psi|^2)\psi, \quad (3.10)$$

⁷Refer to [46] for a detailed derivation of it

where

$$\tau = \tau_{Raman} \sqrt{\frac{\kappa}{2D_2}} D_1 \quad (3.11)$$

is a normalized parameter that takes into account the properties of the resonator and the response of the silica substrate that is of order of femtoseconds and strongly depends on the individual design of the resonator and fabrication.

If we expand this further term in the discrete Fourier basis we can see that it breaks the $\mu \rightarrow -\mu$ -symmetry in a non trivial way. In fact:

$$\begin{aligned} -i\tau\psi\partial_\theta|\psi|^2 &= -i\tau \left(\sum_{\mu} \psi_{\mu} e^{i\mu\theta} \right) \partial_\theta \left(\sum_{\mu',\mu''} \psi_{\mu'} \psi_{\mu''}^* e^{i(\mu'-\mu'')\theta} \right) \\ &= -i\tau \sum_{\mu,\mu',\mu''} \psi_{\mu} \psi_{\mu'} \psi_{\mu''}^* i(\mu' - \mu'') e^{i(\mu+\mu'-\mu'')\theta} \\ &= \tau \sum_{\mu,\mu',\mu''} (\mu' - \mu'') \psi_{\mu} \psi_{\mu'} \psi_{\mu''}^* e^{i(\mu+\mu'-\mu'')\theta} \\ &\Rightarrow \left(\psi_{\eta}, -i\tau\psi\partial_\theta|\psi|^2 \right) = \tau \sum_{\mu,\mu'} (\mu - \eta) \psi_{\mu} \psi_{\mu'} \psi_{\mu+\mu'-\eta}^* \\ &= -\eta\tau \sum_{\mu,\mu'} \psi_{\mu} \psi_{\mu'} \psi_{\mu+\mu'-\eta}^* + \tau \sum_{\mu,\mu'} \mu \psi_{\mu} \psi_{\mu'} \psi_{\mu+\mu'-\eta}^* \end{aligned} \quad (3.12)$$

where with $(\psi_{\eta}, -i\tau\psi\partial_\theta|\psi|^2)$ we consider the projection of the Raman term on a plane wave of mode η . This dependence on the mode number of the equation results in a asymmetry between positive and negative mode numbers and consequently, as simulated, it leads the soliton to acquire an additional detuning dependent group velocity. This can be seen in Fig. 3.3, where, subjected to the same sinusoidal noise as in Fig. 3.1, the soliton is again susceptible to the detuning change.

This time, being simulated the dynamics only in presence of the Raman scattering without any mode displaced, we can see from Fig. 3.3b there is no preferred mode more occupied than others, and consequently no modulation of the background of the soliton. But still the dynamics looks very similar as Fig. 3.1, possibly indicating that the two effects can combine in a optimal way to reduce the noise dependence.

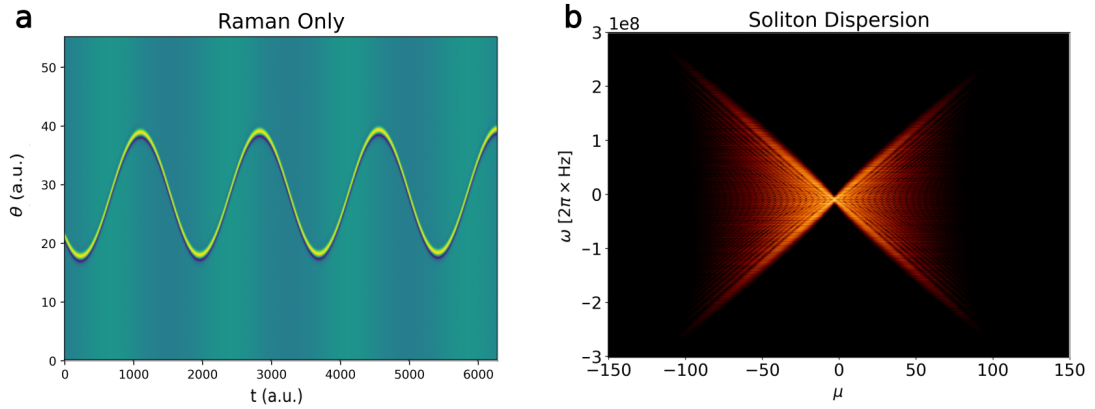


Figure 3.3: Simulation of soliton dynamics in presence of Sinusoidal noise and Raman scattering only. The noise is exactly the same sinusoidal noise as in figure 3.1 but with only Raman scattering present. No resonance for any particular mode indeed and absence of dispersive wave.

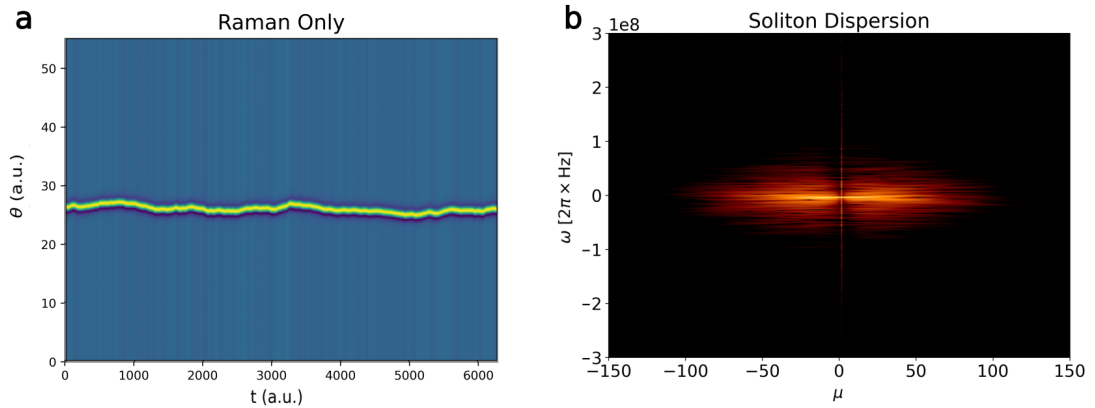


Figure 3.4: Simulation of soliton dynamics in presence of random Lorentian noise and Raman scattering only. Simulation of soliton dynamics in presence of the same random noise as in figure 3.2 but with only Raman scattering present. No resonance for any particular mode indeed and absence of dispersive wave.

3.4 Quiet Point

Combining now both the single mode resonance shift and the Raman term in presence of detuning noise, we looked for the noise reduction effect. By opportunely

sweeping the parameters of the perturbed single mode displaced model (i.e. $a_{\bar{\mu}}$, $\bar{\mu}$) we explored the parameter space to see how the two effects combine together and if this combined effect can lead to a noise reduction, as experimentally proven [45]. We first fixed both the detuning ζ_0 and the resonance shift $a_{\bar{\mu}}$ and simulated the dynamics for different mode number $\bar{\mu}$. Due the Raman term now the dynamics of positive and negative mode are no more related by a parity transformation as in absence of Raman, and for this we needed to simulate the two dynamics independently.

In figure 3.5, we have summed up the major results of the sweeping. By comparing the upper lines of subfigures with the lower one, is evident that there is no more a parity transformation relating the positive and negative dynamics; while in the case of figures 3.5b,d the dynamics are qualitatively the same with some minor differences, in figure 3.5c,e the system dynamics strongly differentiates in the two case, since in one case (cf. Fig. 3.5c) the soliton still responds to the noisy environment, while in the second one (Fig. 3.5e) we can appreciate a clear noise suppression. It is evident from figure 3.5 that the perturbation can both enhance (3.5b,d). or reduce the noise response, until reaching, in the optimal case, the so called quiet operating point (QP)(i.e.the optimal balance between AMX and Raman effects) This has been explained as follows.

Both the perturbations activate a noise transduction mechanism that translates in a detuning-dependent rotation of the soliton linear dispersion; if the rotations induced by the perturbation and by the Raman term are in phase, meaning that they both rotate the soliton line in the same direction, then the system will stronger respond to the detuning noise, enhancing the noisy input. Vice versa, if the perturbations are in antiphase, meaning they tend to rotate the soliton dispersion in opposite direction, we will obtain a reduction (or optimally a complete suppression) of the noise sensitiveness of the system.

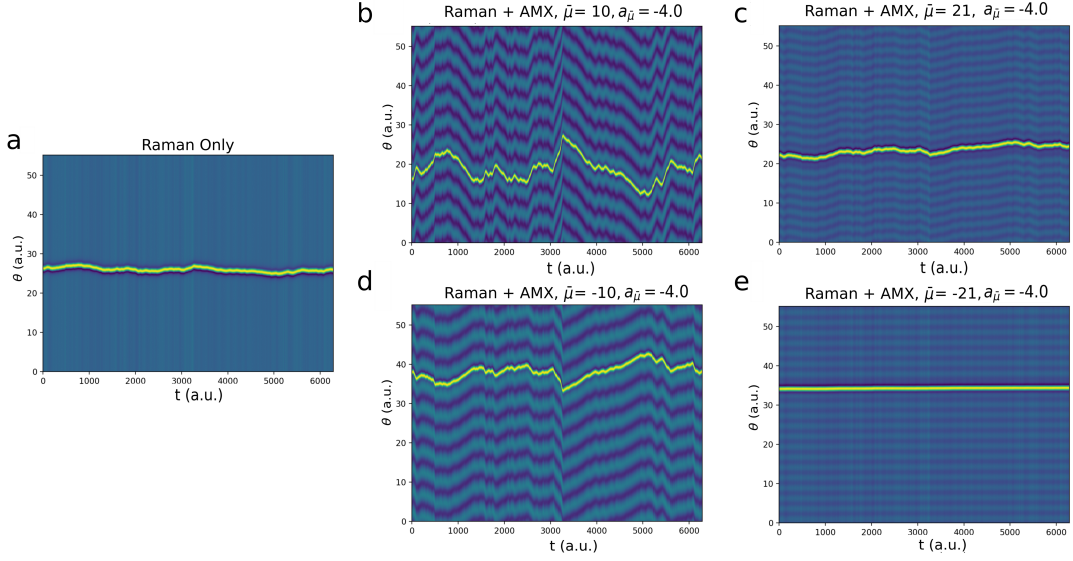


Figure 3.5: Comparison of noise cancellation for different operating points. a) Simulated soliton dynamics in presence of detuning random noise and Raman scattering only. b),c),d),e) Simulated soliton dynamics in presence of exactly the same realization of the random detuning noise present in figure a, computed at different operating points, differing only by the mode number $\bar{\mu}$, in alphabetical order: $\bar{\mu} = 10$, $\bar{\mu} = 21$, $\bar{\mu} = -10$, $\bar{\mu} = -21$.

3.5 Alternative approach to QP

Once it has been demonstrated the possibility of obtaining a QP within the model, the question arise about the uniqueness of this QP; is this the only point in the parameters space having this low sensitiveness on detuning noise or there are more than one?

To answer this question, we applied the same sweeping scheme to a wider region of phase space (sweeping also the detuning and the resonance shift $\zeta_0, a_{\bar{\mu}}$), obtaining some results but at the cost of longer computation time. That is because, to obtain information about the detuning dependence of the soliton dynamics we simulated the complete evolution of it. This is of course a powerful method that completely characterizes the dynamics of the soliton in a given time interval, but due to the richness of information obtained with the simulation, it results as a slow method to observe the different behaviour of the system in a wide region of the space of the parameters. The process of spanning regions of parameters space in search of the quiet operating point should be speed up using a different approach.

The key idea is to find a way to compute the value of the soliton group velocity for

different operating points of the $(\zeta_0, a_{\bar{\mu}}, \bar{\mu})$ -space⁸, without simulating the whole dynamics in presence of noise, and then studying the detuning dependence of the soliton group velocity. This idea is based on the fact that a quiet point is a particular operating point of the parameters space characterised by the lowest dependence on the detuning, regardless on the nature of the noise, being an intrinsic property of the dynamics of system.

To do so, we have implemented the Newton-Raphson method. This method, as explained in more details in chapter 4, it is used to find roots of vectorial equations through an iterative algorithm on subsequent approximations. By opportunely choosing the equations and the unknowns of the equations, it was possible to use it to compute the correct group velocity acquired by the system for a given point of the parameter space, in presence of both the single mode perturbation and the Raman scattering, more than 60 times faster then with the previous method.⁹

3.5.1 Results

Fixing the pump term f for convenience, the parameter space to investigate in search of the quiet points reduces to the three-dimensional space $(\zeta_0, a_{\bar{\mu}}, \bar{\mu})$ making our computed group velocity already a four-dimensional manifold. We then firstly choose to fix the already found mode number $\bar{\mu} = -21$ and sweeping for the parameters in the plane $(\zeta_0, a_{\bar{\mu}})$ and compare it with the case of opposite mode $\bar{\mu} = 21$ resulting in figure 3.6.

From the resulting computation of the group velocity shown in Fig. 3.6, we can see that the soliton group velocity has an increasing (in Fig. 3.6a) (or decreasing in Fig. 3.6b) behaviour toward a specific region of the parameter space and this has been justified by the plot of the occupancy of the displaced mode (cf. Fig. 3.6c,d), showing that a critical value for the group velocity is obtained close to the maximum of the occupied mode. That has been explained by a maximum resonant condition between the soliton and the displaced mode $\bar{\mu}$ for a particular operating point $(\zeta_0, a_{\bar{\mu}})$. Also from this perspective we can see, from the different values in absolute value assumed by the group velocity, how the $P - \mu$ -symmetry presented in chapter 2 is not present anymore.

⁸We remind that we took raman time and pump power fixed

⁹All the details in Chapter 4

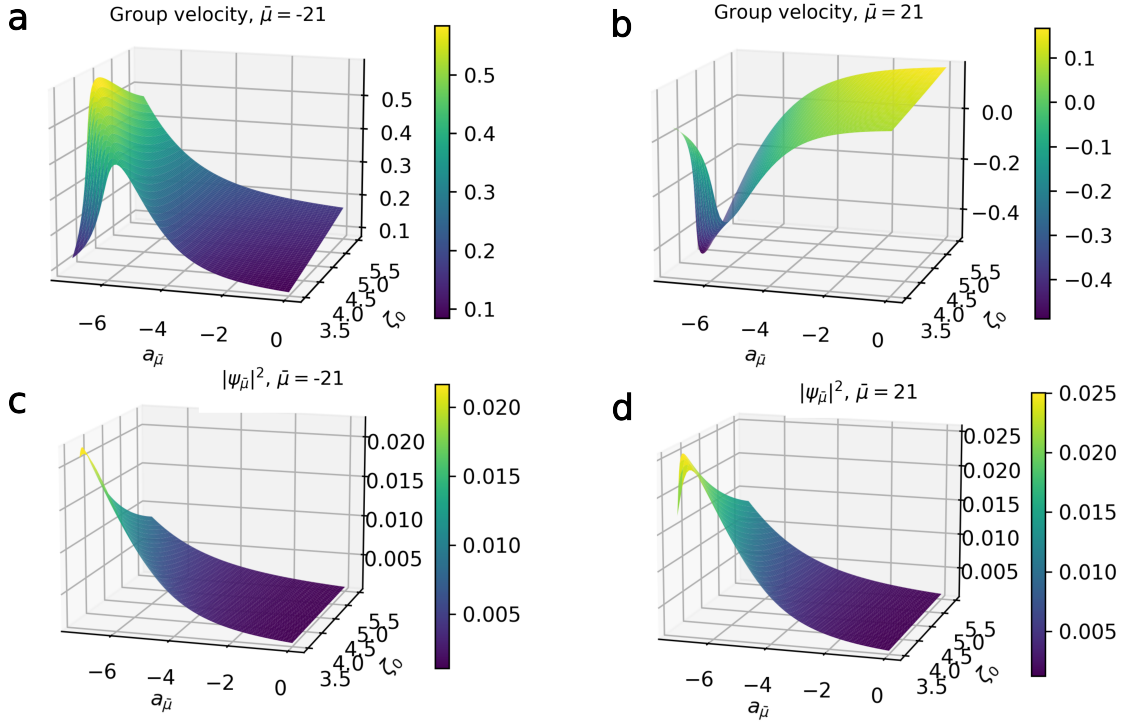


Figure 3.6: Computed soliton group velocities and occupancy of displaced mode in $(\zeta_0, a_{\bar{\mu}})$ -subspace with Newton-Raphson method a) Soliton group velocity for $(\zeta_0, a_{\bar{\mu}}), \bar{\mu} = -21$, b) Soliton group velocity for $(\zeta_0, a_{\bar{\mu}}, \bar{\mu} = 21$, c) Occupancy of displaced mode for $(\zeta_0, a_{\bar{\mu}}, \bar{\mu} = -21$, d) Occupancy of displaced mode for $(\zeta_0, a_{\bar{\mu}}, \bar{\mu} = 21$). We can see that the group velocity and the occupancy of the displaced mode $\bar{\mu}$ present a similar behaviour. To note that, due to the presence of Raman term, we have the breaking of $P - \mu$ -symmetry obtaining that $v_{g, \bar{\mu} > 0} \neq -v_{g, \bar{\mu} < 0}$

At this point, we searched for the quiet points by numerically computing the directional derivative of the group velocity w.r.t the detuning direction (3.7), since a QP can be identified as a point $P = (\zeta_0^*, a_{\bar{\mu}}^*, \bar{\mu}^*)$ such that:

$$\frac{\partial v_g}{\partial \zeta_0} \Big|_P = 0 \quad (3.13)$$

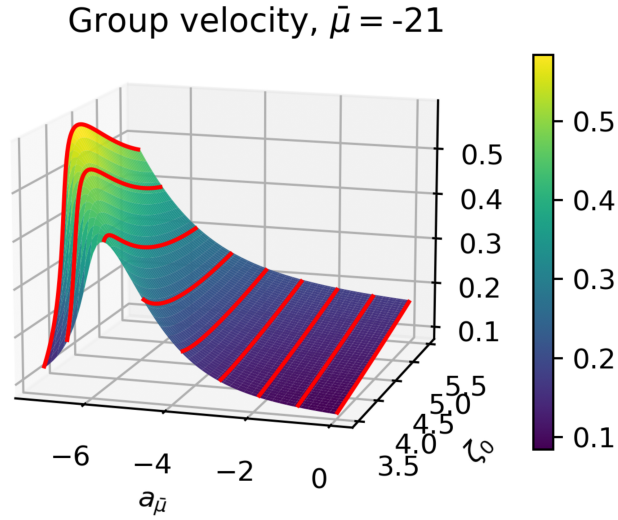


Figure 3.7: Example of fixed detuning lines for derivative computation in the case of subfigure a) of fig. 3.6

The computation of the derivatives are shown in 3.8 in log10 scale.

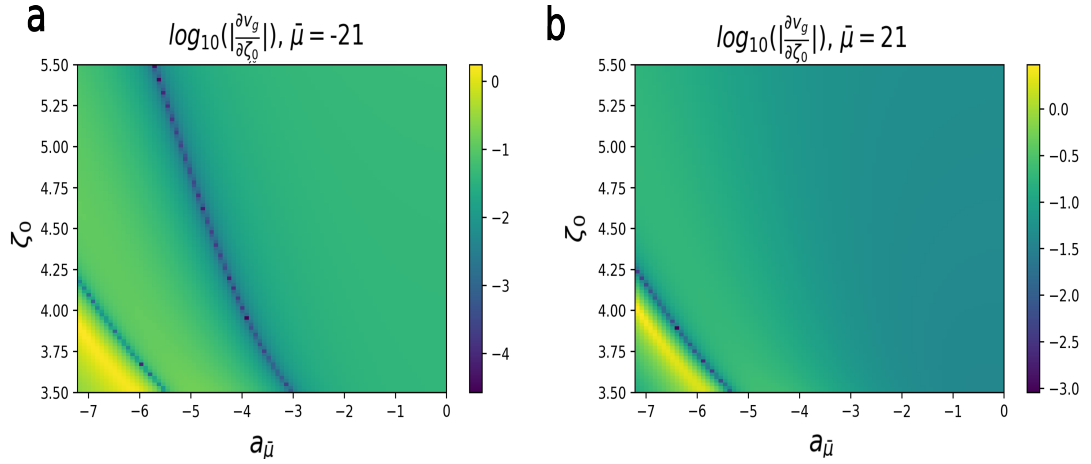


Figure 3.8: Directional derivative of soliton group velocity along the ζ_0 -direction (i.e. detuning). Log₁₀ value of the directional derivatives along the detuning direction of the group velocities of figure 3.6, with subfigures in the same order. It is clear the difference between positive and negative mode, since the latter present a further line of quiet points.

We can see that the two cases present both some common features and some different ones. First of all, in both the cases the derivatives present, in the bottom

left corner of the region of parameters, two lines of points of opposite behaviour; The yellow line, that is characterized by high values of the derivative in which we expect the system to be strongly dependent on the detuning, and the blue line, in which we have an opposite behaviour, characterized by low value of the derivative. The points on this latter line can be already considered quiet points, verifying already the existence of different quiet points.

We notice that these two lines can be related to the occupancy of the displaced mode being in proximity of its maximum (see Fig. 3.6). Furthermore, an important difference is evident in Fig. 3.8: the negative mode clearly manifests a further line of QPs that is absent in the positive mode case. This difference has again to be understood due to the Raman scattering that breaks the $P - \mu$ -symmetry.

From this result we could apriori predict the simulations shown in Fig. 3.5c,d ($P_c = (4, -4, 21)$, $P_d = (4, -4, -21)$). In fact in the first case (P_c) the operating point is in the green region of figure 3.8b with no particular noise reduction, whereas P_d stays exactly on the QP lines.

Furthermore, this latter line of QPs, differently from the first one in the bottom corner, being far from region of high enhancement of the noise, should be the preferred one in the engineering of a device, since, due to some fabrication errors, in this case even if the point would not be one of the quietest, it still will be in a region of low derivative (i.e. low noise sensitiveness), while in the case of the corner QP line, a fabrication error could result in operating the system in a region of high enhancement of the noise, resulting in a bad performing device.

To double check the correctness of the approach, we launched a further test, running three complete simulations of the dynamics in presence of random noise at fixed detuning for the operating points shown in figure 3.9.

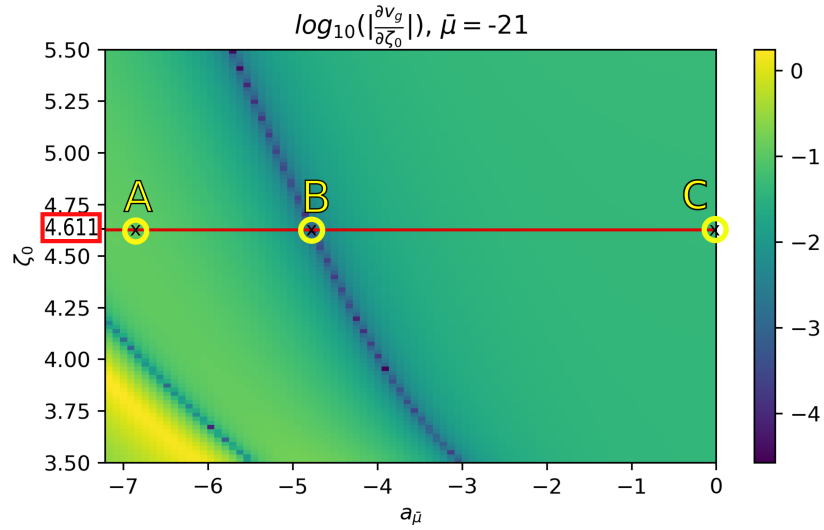


Figure 3.9: Choosing the operating points on the group velocity change plot for further investigation of the noise properties.

The results are plotted in figure 3.10. With these further simulations we have clearly observed that the lines in parameter space really coincides to a quiet points line, demonstrating the existences of multiple quiet points for different realizations of the mode shifting.

This is a brand new results, since in the literature it has never been considered the possibility of having different quiet points, opening the scenario of engineering the system to beside exactly at the more convenient quiet point.

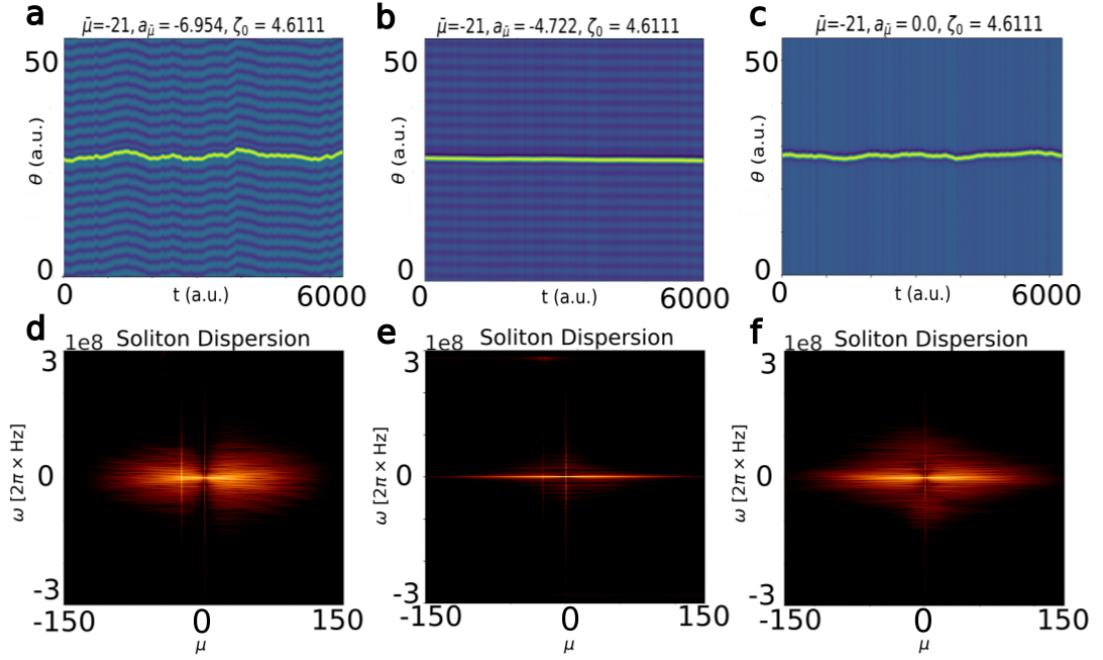


Figure 3.10: Resulting simulations related to fig.3.9

3.5.2 Analytical Derivation

Considered the crucial role of the quiet operating point in the generation of ultra-low noise RF signal and thus the potential impact of the numerical simulations presented in the previous sections, finally we tried to analytically derive the results shown in Fig. 3.8 in order to extend the considerations directly from a closed form equation.

To do so, we followed the common procedure to study the properties of the solution of perturbed Nonlinear Schrödinger Equations (NLSE) [36], by substituting an ansatz solution in the definition of the norm (2.10) and momentum (2.12). We took as an ansatz a soliton solution of the unperturbed NLSE with an additional superposition of a plane wave of period $\bar{\mu}$ and amplitude proportional to $a_{\bar{\mu}}$, locked to the soliton pulse, as the numerical observations showed 2.3:

$$\psi = B \operatorname{sech} \left(\frac{\theta - \theta_0}{\tau_s} \right) e^{i\varphi} e^{-i\Omega(\theta - \theta_0)} + a_{\bar{\mu}} A e^{i\bar{\mu}(\theta - \theta_0)} e^{i\varphi} \quad (3.14)$$

Equations (2.10) and (2.12) are then rewritten as follows:

$$\begin{aligned}
 N &= \int d\theta |\psi|^2 \\
 &= \int d\theta \left[B^2 \operatorname{sech}^2 \left(\frac{\theta - \theta_0}{\tau_s} \right) + a_{\bar{\mu}}^2 A^2 + 2a_{\bar{\mu}} AB \Re \{ e^{i((\Omega + \bar{\mu})(\theta - \theta_0))} \} \operatorname{sech} \left(\frac{\theta - \theta_0}{\tau_s} \right) \right] \\
 &= 2B^2 + a_{\bar{\mu}}^2 A^2 L + 2a_{\bar{\mu}} AB \tau_s \Re \int dx \operatorname{sech}(x) e^{i(\Omega + \mu)\tau_s x} \\
 &= 2B^2 + a_{\bar{\mu}}^2 \bar{\mu} A^2 L + 2a_{\bar{\mu}} AB \pi \operatorname{sech} \left[\frac{\pi}{2} (\Omega + \bar{\mu}) \tau_s \right]
 \end{aligned} \tag{3.15}$$

$$\begin{aligned}
 P &= 2\Im \int d\theta \psi^* \partial_\theta \psi = 2\Im \int d\theta e^{i\varphi} \psi^* \partial_\theta \psi e^{-i\varphi} \\
 &= 2\Im \int d\theta \psi^* \partial_\theta \left[B \operatorname{sech} \left(\frac{\theta - \theta_0}{\tau_s} \right) e^{-i\Omega(\theta - \theta_0)} + a_\mu A e^{i\bar{\mu}(\theta - \theta_0)} \right] \\
 &= 2\Im \int d\theta \psi^* \left[\frac{B}{\tau_s} (-) \operatorname{sech} \left(\frac{\theta - \theta_0}{\tau_s} \right) \tanh \left(\frac{\theta - \theta_0}{\tau_s} \right) e^{-i\Omega(\theta - \theta_0)} \right. \\
 &\quad \left. - i\Omega B \operatorname{sech} \left(\frac{\theta - \theta_0}{\tau_s} \right) e^{-i\Omega(\theta - \theta_0)} + i\bar{\mu} a_\mu A e^{i\bar{\mu}(\theta - \theta_0)} \right] \\
 &= 2\Im \int d\theta \left[-\frac{B^2}{\tau_s} \operatorname{sech}^2 \left(\frac{\theta - \theta_0}{\tau_s} \right) \tanh \left(\frac{\theta - \theta_0}{\tau_s} \right) - i\Omega B^2 \operatorname{sech}^2 \left(\frac{\theta - \theta_0}{\tau_s} \right) \right. \\
 &\quad \left. + i\bar{\mu} a_\mu A B \operatorname{sech} \left(\frac{\theta - \theta_0}{\tau_s} \right) e^{i(\Omega + \bar{\mu})(\theta - \theta_0)} \right. \\
 &\quad \left. - a_\mu A \frac{B}{\tau_s} \operatorname{sech} \left(\frac{\theta - \theta_0}{\tau_s} \right) \tanh \left(\frac{\theta - \theta_0}{\tau_s} \right) e^{-i(\bar{\mu} + \Omega)(\theta - \theta_0)} \right. \\
 &\quad \left. - i\Omega a_\mu A B \operatorname{sech} \left(\frac{\theta - \theta_0}{\tau_s} \right) e^{-i(\mu + \Omega)(\theta - \theta_0)} + i\bar{\mu} a_\mu^2 A^2 \right] \\
 &= 2\Im \left\{ -i\Omega B^2 \int d\theta \operatorname{sech}^2 \left(\frac{\theta - \theta_0}{\tau_s} \right) + i\bar{\mu} a_\mu A B \int d\theta \operatorname{sech} \left(\frac{\theta - \theta_0}{\tau_s} \right) e^{i(\Omega + \bar{\mu})\tau_s \frac{\theta - \theta_0}{\tau_s}} \right. \\
 &\quad \left. + a_\mu A B \int d\theta \partial_\theta \operatorname{sech} \left(\frac{\theta - \theta_0}{\tau_s} \right) e^{-i(\bar{\mu} + \Omega)\tau_s \frac{\theta - \theta_0}{\tau_s}} \right. \\
 &\quad \left. - i\Omega a_\mu A B \int d\theta \operatorname{sech} \left(\frac{\theta - \theta_0}{\tau_s} \right) e^{-i(\bar{\mu} + \Omega)\tau_s \frac{\theta - \theta_0}{\tau_s}} + i\bar{\mu} a_\mu^2 A^2 \int d\theta \right\} \\
 &= -4\Omega B^2 + 2\bar{\mu} a_\mu A B \tau_s \pi \operatorname{sech} \left(\frac{\pi}{2} (\Omega + \bar{\mu}) \tau_s \right) + 2\bar{\mu} a_\mu^2 A^2 L \\
 &\quad - 2\Omega a_\mu A B \tau_s \operatorname{sech} \left(\frac{\pi}{2} (\Omega + \bar{\mu}) \tau_s \right) \pi + 2(\bar{\mu} + \Omega) a_\mu A B \tau_s \pi \operatorname{sech} \left(\frac{\pi}{2} (\Omega + \bar{\mu}) \tau_s \right) \\
 &= -4\Omega B^2 + 2\bar{\mu} a_\mu^2 A^2 L + 4\pi \bar{\mu} a_\mu A B \tau_s \operatorname{sech} \left(\frac{\pi}{2} (\Omega + \bar{\mu}) \tau_s \right)
 \end{aligned} \tag{3.16}$$

The group velocity of the soliton is then proportional to[36]:

$$v_g \propto \frac{P}{N} = \frac{-4\Omega B^2 + 2\bar{\mu} a_\mu^2 A^2 L + 4\pi \bar{\mu} a_\mu A B \tau_s \operatorname{sech} \left(\frac{\pi}{2} (\Omega + \bar{\mu}) \tau_s \right)}{2B^2 + a_\mu^2 \bar{\mu} A^2 L + 2a_\mu A B \pi \operatorname{sech} \left(\frac{\pi}{2} (\Omega + \bar{\mu}) \right)} \tag{3.17}$$

Assuming now the following:

$$\tau_s = \frac{1}{B} \quad (3.18)$$

$$B = \sqrt{2(\zeta_0 + \gamma a_{\bar{\mu}})} \quad (3.19)$$

$$\Omega = -\frac{16}{15} \tau \frac{B^2}{\tau_s^2} \quad (3.20)$$

$$\partial_{\zeta_0} A = 0 \quad (3.21)$$

Where the first two relations are obtained from the unperturbed NLSE soliton solution[36]the third one from a Lagrangian approach in presence of only Raman scattering [47] and the last one from the numerical simulations. In particular in 3.19 we also took in account a correction term ($\gamma a_{\bar{\mu}}$) depending on the parameter of perturbation. Assuming additionally that:

$$\partial_{\zeta_0} P \gg \partial_{\zeta_0} N \quad (3.22)$$

as numerical simulations showed in presence of noise, we obtained:

$$\partial_{\zeta_0} v_g = \frac{\frac{G\sqrt{1-G^2}(2\pi^2 A \bar{\mu}^2 a_{\bar{\mu}})}{\sqrt{2z^{3/2}}} + \frac{8}{5}\pi^2 AG\sqrt{1-G^2}\bar{\mu}\tau a_{\bar{\mu}}\sqrt{z} + \frac{128}{5}\tau z^2}{A^2 L a_{\bar{\mu}}^2 + 2\pi A G a_{\bar{\mu}} \sqrt{2z} + 4z} \quad (3.23)$$

With:

$$\begin{aligned} z &= \zeta_0 + \gamma a_{\bar{\mu}} \\ \Xi &= \frac{\pi \left(\bar{\mu} - \frac{16}{15} \tau z^2 \right)}{2\sqrt{2z}} \\ G &= \text{sech}(\Xi) \\ A &= 0.01 \\ \gamma &= 0.57 \\ \tau &= 0.005 \\ L &= 200 \end{aligned}$$

Where the values of the parameters A, γ, L have been fitted in order to reproduce a comparable results.

From figures 3.11 and 3.12 we can see a comparison between the numerical (3.11a,b) the analytical (3.11,c,d). The figures show that within the analytical formulation is possible to catch the main properties of the system, such as the different behaviour between positive and negative mode numbers $\bar{\mu}$ and, more importantly, the quiet points lines.

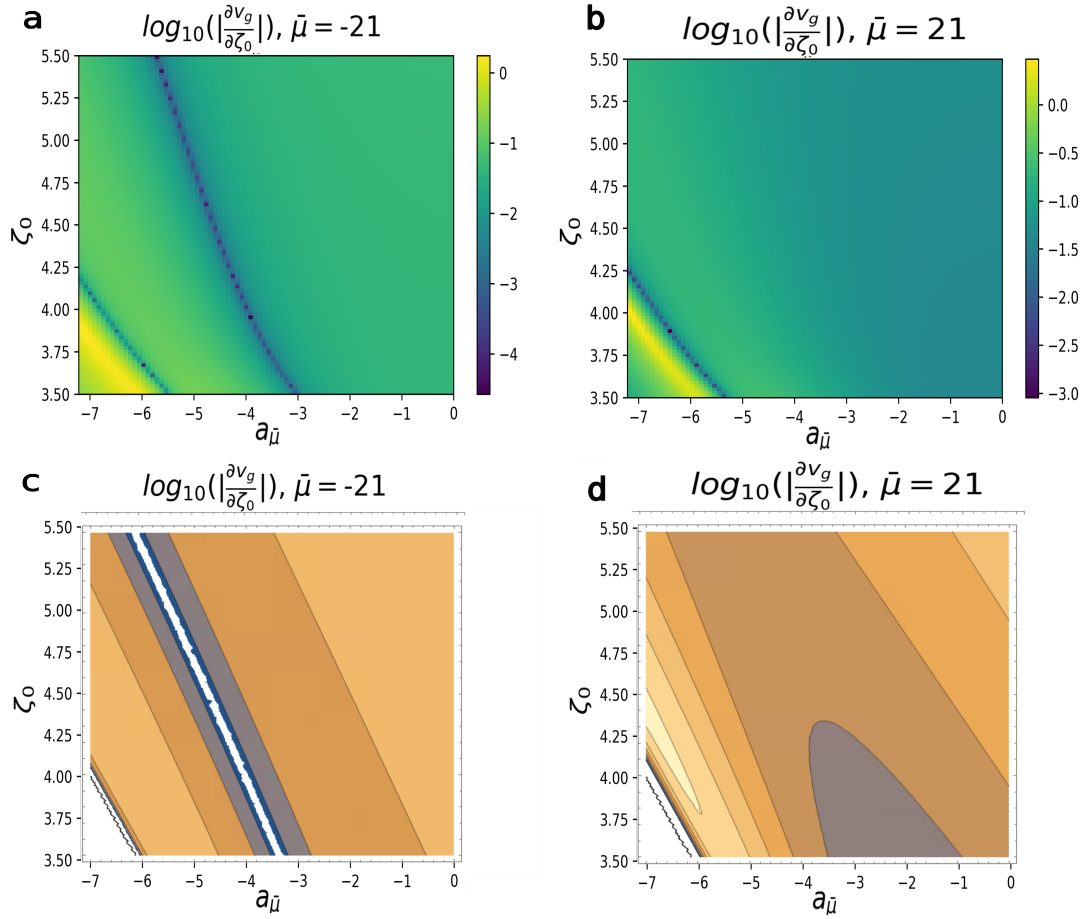


Figure 3.11: Comparison between the numerical (left) and analytical (right) values of the log-derivative of the group velocity.

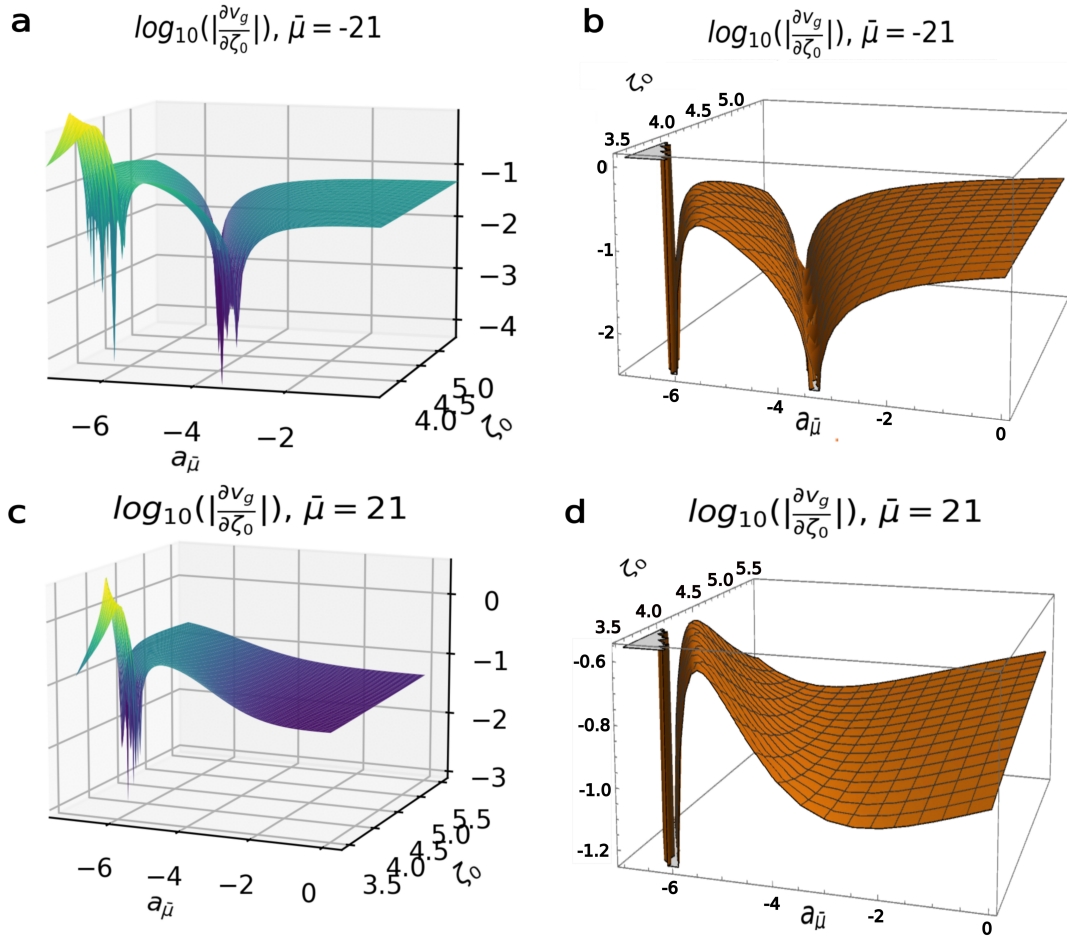


Figure 3.12: Comparison between the numerical (left) and analytical (right) 3D plots of the soliton (log-)group velocity $\log_{10}(|\partial_{\zeta_0} v_g|)$. We can see how the analytical formula predicts the different behaviours for opposite values of $\bar{\mu}$.

Chapter 4

Numerical Methods

To study the dynamical properties of the systems two different numerical approach have been used in this work, the Split-Step method and a generalization of Newton-Raphson method. The first one has been used to simulate the dynamics of the system finding numerical solutions of the perturbed LLE (3.10), not being known any analytical solution of it.

The second one instead has been implemented to obtain insights on the response of the system in presence of frequency noise to find the optimal values satisfying the quiet point (QP) conditions.

In the following a general description of each method is proposed, followed by the actual implementation for the particular problems considered.

4.1 Split-Step Algorithm

Considering a general nonlinear partial differential equations (PDE) of the first order in time and with explicit derivative term w.r.t time. Then it can be formally written as:

$$\partial_t \psi = \hat{H} \psi := [\hat{D} + \hat{N}] \psi \quad (4.1)$$

where we separated the infinitesimal evolution operator \hat{H} in its linear, \hat{D} , and nonlinear part, \hat{N} . The equation is formally solved by the action of the propagator on the initial condition i.e.:

$$\partial_t \psi = [\hat{D} + \hat{N}] \psi \Rightarrow \psi(t) = \hat{U}(t) \psi(0) \quad (4.2)$$

where, $\hat{U}(t) := e^{[\hat{D} + \hat{N}]t}$.

In the optimal case in which the linear and nonlinear operators commute (i.e.

$[\hat{D}, \hat{N}] = 0$) the propagator can be factorized in two independent ones as follows:

$$\hat{U}(t) = e^{[\hat{D}+\hat{N}]t} = e^{\hat{D}t}e^{\hat{N}t} \quad (4.3)$$

So, if the nonlinear propagator (i.e. $e^{\hat{N}t}$) can be analytically computed¹, the PDE is solved by firstly evolving the initial condition applying one propagator and subsequently applying the other one:

$$\psi(t) = \hat{U}(t)\psi(0) = e^{\hat{D}t}e^{\hat{N}t}\psi(0) \quad (4.4)$$

This is not always the case since in general the operators \hat{D} and \hat{N} do not commute, i.e. $[\hat{D}, \hat{N}] \neq 0$.

However, for two general operators we can write as follows thanks to the Baker–Campbell–Hausdorff formula[[wiki](#)]:

$$e^{\hat{D}t}e^{\hat{N}t} = e^{(\hat{D}+\hat{N})t + \frac{t^2}{2}[\hat{D}, \hat{N}] + g([\hat{D}, \hat{N}], t)} \quad (4.5)$$

$$\hat{g}(0, t) = 0 \quad (4.6)$$

$$\hat{g}([\hat{D}, \hat{N}], t) = O(t^3) \quad (4.7)$$

where for (4.7) it has further assumed that operators \hat{D} and \hat{N} do not explicitly depends on time.

In the present work it has been adopted one of the simplest implementation of the Split-Step method to simulate (3.10); this is based on the assumption that for small enough time interval, the propagator can be factorized² owing an error of order t^2 , due to the first neglected term in exponent of (4.5).

In formulas:

$$\hat{U}(\delta t) = e^{(\hat{D}+\hat{N})\delta t} \approx e^{\hat{D}\frac{\delta t}{2}}e^{\hat{N}\frac{\delta t}{2}} \quad (4.8)$$

$$\psi(N\delta t) = \prod_{i=1}^N (e^{\hat{D}\frac{\delta t}{2}}e^{\hat{N}\frac{\delta t}{2}})\psi(0) \quad (4.9)$$

Note that this method is faster than the finite difference relying on the optimized Fast Fourier Transform (FFT) algorithm.

¹A linear propagator can be always in principle formally derived

²That is equivalent of assuming the propagation media as stratified in subsequent layers of nonlinear and linear material

4.2 Simulation of perturbed LLE

As described in chapter 3 the system under study is described by the following PDE:

$$\partial_t \psi = -(1 + i\zeta_0)\psi + \frac{i}{2}\partial_\theta^2 \psi + i|\psi|^2\psi - i\tau(\partial_\theta|\psi|^2)\psi + f - ia_{\bar{\mu}}\psi_{\bar{\mu}}e^{i\bar{\mu}\theta} \quad (4.10)$$

Following the Split-step algorithm, we have first to solve independently the following linear and nonlinear PDEs (i.e. finding the respective propagators $e^{\hat{D}t}$ and $e^{\hat{N}t}$):

$$\partial_t \psi = \hat{D}\psi \equiv -(1 + i\zeta_0)\psi + \frac{i}{2}\partial_\theta^2 \psi + f - ia_{\bar{\mu}}\psi_{\bar{\mu}}e^{i\bar{\mu}\theta} \quad (4.11)$$

$$\partial_t \psi = \hat{N}\psi \equiv i|\psi|^2\psi - i\tau(\partial_\theta|\psi|^2)\psi = i[(1 - \tau\partial_\theta)|\psi|^2]\psi \quad (4.12)$$

As for (4.11), being a linear equation we can solve it in Fourier space, where it reads as follows:

$$\partial_t \psi_\mu = -(1 + iZ_{\mu,\bar{\mu}})\psi_\mu + f \quad (4.13)$$

with $Z_{\mu,\bar{\mu}} := \zeta_0 + \frac{\mu^2}{2} + a_{\bar{\mu}}\delta_{\mu,\bar{\mu}}$. This is a first order nonhomogenous linear differential equation and the solution is readily found as the following:

$$\psi_\mu(t) = e^{-(1+iZ_{\mu,\bar{\mu}})t}\psi_\mu(0) + \frac{f}{(1+iZ_{\mu,\bar{\mu}})}(1 - e^{-(1+iZ_{\mu,\bar{\mu}})t}) \quad (4.14)$$

Defining now the operator $\hat{O}_{\mu,\bar{\mu}}$ as follows:

$$\hat{O}_{\mu,\bar{\mu}}(t)\psi := e^{-(1+iZ_{\mu,\bar{\mu}})t}\hat{\mathcal{F}}\psi + \frac{f}{(1+iZ_{\mu,\bar{\mu}})}(1 - e^{-(1+iZ_{\mu,\bar{\mu}})t}) \quad (4.15)$$

we can express the propagator of the linear equation as:

$$e^{\hat{D}t} = \hat{\mathcal{F}}^{-1}\hat{O}_{\mu,\bar{\mu}}(t) \quad (4.16)$$

where with $\hat{\mathcal{F}}(\hat{\mathcal{F}}^{-1})$ we considered the operator that Fourier-(anti)transform an \mathcal{L}^2 function.

Owing to the translation invariance of the system, being the system in a ring geometry, we do not have to bother for the implementation of the periodic boundary conditions in the code that are automatically implemented by the use of the Fourier transform.

Concerning now the nonlinear equation (4.12), it can be easily solved once noticed that $\partial_t|\psi|^2 = 0$.

In fact, multiplying eq. (4.12) by ψ^* we obtain:

$$\psi^*\partial_t\psi = i[(1 - \tau\partial_\theta)|\psi|^2]|\psi|^2 \quad (4.17)$$

summing now (4.17) to its complex conjugated we obtain:

$$\psi^* \partial_t \psi + \psi \partial_t \psi^* \equiv \partial_t |\psi|^2 = i[(1 - \tau \partial_\theta) |\psi|^2] |\psi|^2 - i[(1 - \tau \partial_\theta) |\psi|^2] |\psi|^2 = 0 \quad (4.18)$$

Thanks to this result we can readily write the propagator of (4.10) as:

$$e^{\hat{N}t} = e^{i[(1 - \tau \partial_\theta) |\psi|^2]t} \quad (4.19)$$

Once the two propagator have been computed, we it has been possible to follow the Split-Step algorithm, implementing it in a C++ program.

4.2.1 Hard and Soft Seed

To simulate the dynamics two different types of initial conditions (i.e. seeds) have been selected. We refer as soft seed when the dynamics has been initialized with a zero initial condition, i.e. the initial field inside the resonator has zero amplitude. This type of seed is used to simulate the actual experiment of exciting the resonator, in which the laser frequency (i.e. detuning) is adiabatically increased over time, until the first resonance frequency of the cavity is reached and the four-wave mixing processes are started³.

The requirement of adiabaticity in the evolution of the detuning term is to assume the system can be described to at any instant by equation (4.10) with fixed detuning ζ_0 .

It has been implemented as follows. Being ζ_n the detuning at time t_n , assuming a linear increase with time of the detuning, we have:

$$\zeta_n = \zeta_{n-1} + \delta\zeta \quad (4.20)$$

$$t_n = t_{n-1} + \delta\tau \quad (4.21)$$

The adiabaticity conditon is assumed such that⁴:

$$\frac{\delta\zeta}{\delta\tau} \ll 1 \quad (4.22)$$

. An hard seed is instead an initial condition for the field inside the resonator of a particular shape that could be represented by a particular state of the system, to study the dynamics of the particular state; the majority of the simulations in

³also said scanning through the resonance

⁴We are assuming normalized parameters

the work have been done with an hard seed represented by an approximated single soliton solution obtained as follows:

$$\psi(0) = \psi_0 + B \operatorname{Sech}(B(\theta - \theta_0))e^{i\varphi} \quad (4.23)$$

with:

$$\psi_0 = \frac{f}{1 + i\zeta_0} \quad (4.24)$$

$$B = \sqrt{2\zeta_0} \quad (4.25)$$

$$\cos(\varphi) = \frac{\sqrt{8\zeta_0}}{\pi f} \quad (4.26)$$

where (4.24) is the uniform constant solution of (4.10), while equation of the shape, of the modulus and of the phase are the one obtained within a Lagrangian approach in the case of simple LLE⁵.

As it can be seen from its definition, the seed depends on the particular operating point of the parameters space chosen. It means that if there is a mismatch between the initial values of the simulation parameters and those at which the seed is referred to, the solitonic seed will hardly be stable and will decay to the uniform solution. Figures

4.2.2 Faraday Instability

As highlighted in the footnote2 of this chapter, the implementation of this algorithm is based on a simplified assumption that see the medium in which the light propagate as a stratified medium with subsequent layers of linear and nonlinear materials, where the size of each layer is given by the time interval separating two subsequent instant of time $\delta\tau$.

If this interval is not small enough, the result is that the simulation will start feeling the periodicity of the medium, manifesting the so called Faraday instability. This numerical artifact is defined as an instability since it destabilizes the solitonic solution.

To avoid this numerical error the time interval has been fixed running multiple hard seeded simulations with different values of $\delta\tau$ for long propagation times and see for which one the soliton remained stable.

⁵See results chapter ? for τ and $\delta\zeta_{\bar{\mu}}$ and $\bar{\mu}$ equal to zeros

4.2.3 Soliton Noisy dynamics simulation

The same method has been used to simulate the soliton dynamics in presence of detuning noise according to equation (3.10).

The procedure has been exactly the same discussed in Subsection 4.2.1, where a single soliton solution has been hard seeded with the key difference that the detuning array this time has not considered constant but it has been obtained as a realization of a stochastic process defined by the following equation:

$$\zeta(t) = \zeta_0 + \delta\zeta(t) \quad (4.27)$$

$$\delta\zeta(t) = \int d\omega \tilde{\delta\zeta}(\omega) e^{i(\omega t + x(\omega))} \quad (4.28)$$

$$x \sim U_{[-\pi, \pi]} \quad (4.29)$$

where $\tilde{\delta\zeta}(\omega)$ represents the zero-mean spectral density of the detuning noise, incoherently superimposed thanks to the random uniformly distributed phase x , in order to generate a random detuning noise array. Two types of spectral density have been considered in the simulations.

A first type taken as a test defined as a Lorentian with parameters chosen such that the standard deviation of the detuning noise was of the order of the 10% of the mean value ζ_0 .

The second type is instead obtain from the actual power spectral density of the detuning noise of the Toptica laser. At the end, as demonstrated in chapter 3, the nature of the quiet point of operation is an intrinsic property of the system to be the more insensitive as possible to variations of detuning, independently⁶ on how it is distributed.

4.3 Newton-Raphson Method

The Newton-Raphson method, is a method used to find roots of nonlinear equations starting from an initial guess, through an iterative algorithm on subsequent approximations. It can also be used to find constant solutions of ordinary differential equation, finding a numerical root of the system of equations expressed in explicit form. In the work it has been used for computing the behaviour of the group velocity depending on the operating point in a subspace of parameters space, in order to find the condition for a quiet point⁷. After a short description of the algorithm, in the following the application to the perturbed equation (3.10) are discussed in detail.

⁶Excluding critical case of relatively big standard deviation

⁷see chapter 3

4.4 General description of the method

Let:

$$\underline{F}(\underline{\Psi}) = 0 \quad (4.30)$$

representing a set of nonlinear equations to integrate and $\underline{\hat{J}}(\underline{\Psi})$ the corresponding Jacobian⁸ defined as follows:

$$\underline{\hat{J}}(\underline{\Psi}) \underline{\delta\Psi} := \underline{F}^{Lin.}(\underline{\Psi} + \underline{\delta\Psi}) - \underline{F}(\underline{\Psi}) \quad (4.31)$$

Where with $\underline{F}^{Lin.}$ we indicate first order approximation of $\underline{F}(\underline{\Psi} + \underline{\delta\Psi})$ in $\underline{\delta\Psi}$. The method is based on the following iteration scheme:

$$\begin{cases} \underline{\Psi}^{(k+1)} = \underline{\Psi}^{(k)} - \underline{\hat{J}}^{-1}(\underline{\Psi}^{(k)})\underline{F}(\underline{\Psi}^{(k)}) \\ \underline{\Psi}_0 : \text{Initial guess solution} \end{cases} \quad (4.32)$$

With $\underline{\hat{J}}^{-1}$ the inverse of the matrix $\underline{\hat{J}}$.

Assuming the conditions such that $\underline{\hat{J}}^{-1}$ exists, the solution is given by the fixed point $\underline{\Psi}^*$ of the iteration⁹.

To implement the algorithm for a continuous case (as the one required by the work), it is necessary to correctly discretize all the variables, since the roots to look for can be continuous functions, solutions of differential equation.

To discretize the function we use the standard approach of discretize the domain of the function into N equal intervals and take the array $\underline{\Psi}^{discr.}$ whose components are the values of the function in the middle points of the discretized domain.

Once the function has been discretized in an array form, a matrix equation of the following form :

$$\underline{\mathbf{F}} \underline{\Psi}^{discr.} = 0 \quad (4.33)$$

has to be found, describing the equation (4.30), where $\underline{\mathbf{F}}$ is a discrete matrix representation of the nonlinear function \underline{F} and analogously a matricial representation $\underline{\hat{\mathbf{J}}}$ of the Jacobian matricial operator has to be obtained¹⁰.

⁸In case of differential equations, as the one in which we are interested, it can be a matricial operator

⁹For more details refer to [48]

¹⁰Both these matrices will depend in principle on the solution itself, as also readable from the description of the iteration scheme

Furthermore, a threshold value has to be fixed to define the convergence and to stop the iteration.

This is done defining a metrics to compare the solutions at two subsequent iterations.

In the present work the threshold has been chosen as the relative error computed with a 2-norm:

$$\epsilon = \sqrt{\sum_{i=1}^N \left| \frac{\Psi_{k+1}^{(i)} - \Psi_k^{(i)}}{\Psi_k^{(i)}} \right|^2} \quad (4.34)$$

and the convergence criterion has been fixed as:

$$\epsilon < 10^{-6} \quad (4.35)$$

4.4.1 Soliton Group Velocity Implementation: Equations

As described in Chapter 3, to overcome the slowness of the Split-step method related to the computation of the group velocity acquired by the system, we implemented the Newton-Raphson method.

In the following the implementation of the method has been explained.

Considering the equation (3.10) here rewritten for convenience¹¹:

$$\partial_t \psi = -(1 + i\zeta_0)\psi + \frac{i}{2}\partial_\theta^2 \psi + i|\psi|^2 \psi - i\tau(\partial_\theta |\psi|^2)\psi + f - ia_{\bar{\mu}}\psi_{\bar{\mu}}e^{i\bar{\mu}\theta} \quad (4.36)$$

The method can be applied thanks to the conservation of the momentum of the system.

Since the velocity acquired by the soliton is constant, in fact, the idea is to set the algorithm such that it will find the correct reference frame (i.e. the constant velocity) in which the equation admits a stationary solution.

This is equivalent to find solution of the equation in the form of propagating wave at constant velocity as follows:

$$\psi(t, \theta) = \psi(\theta - v_g t) \quad (4.37)$$

In this way, the l.h.s. of equation (4.36) is rewritten as:

$$\partial_t \psi = -v_g \partial_\theta \psi \quad (4.38)$$

¹¹Since as already stated, the position of the quiet points does not depend on the particular distribution of the detuning noise but only on its mean value defining the actual operating point, only the noiseless equation must be considered

And the equation is now rewritten as follows:

$$-(1 + i\zeta_0)\psi + v_g\partial_\theta\psi + \frac{i}{2}\partial_\theta^2\psi + i|\psi|^2\psi - i\tau(\partial_\theta|\psi|^2)\psi + f - ia_{\bar{\mu}}\psi_{\bar{\mu}}e^{i\bar{\mu}\theta} = 0 \quad (4.39)$$

To correctly apply the method to find the group velocity v_g , as clear from (4.32), we should be able to compute the equation at each iteration, and that requires to know, in addition to the group velocity, also the value of the field ψ in any point, requiring to consider it as a further variable the algorithm has to find. Furthermore, since ψ and ψ^* are independent (conjugated) variables, we have to consider in the array of solutions also ψ^* .

In this way we define the array of solution we want the algorithm to converge as the following:

$$\underline{\Phi}' = \begin{bmatrix} \psi \\ \psi^* \\ v_g \end{bmatrix} \quad (4.40)$$

Having increased the number of unknown of our problem we should add also two further equations to obtain a well determined problem. A second equation that can be readily written is the conjugated of equation (4.39) obtaining the following system of equations:

$$\begin{cases} -(1 + i(\zeta_0 - \frac{1}{2}\partial_\theta^2))\psi + i\psi(1 - \tau\partial_\theta)|\psi|^2 + f - ia_{\bar{\mu}}\psi_{\bar{\mu}}e^{i\bar{\mu}\theta} + v_g\partial_\theta\psi = 0 \\ -(1 - i(\zeta_0 - \frac{1}{2}\partial_\theta^2))\psi^* - i\psi^*(1 - \tau\partial_\theta)|\psi|^2 + f + ia_{\bar{\mu}}\psi_{\bar{\mu}}^*e^{-i\bar{\mu}\theta} + v_g\partial_\theta\psi^* = 0 \end{cases} \quad (4.41)$$

The last missing equation has been instead written requiring that the position of the maximum of the (soliton) solution at each iteration does not evolve with time. This has been expressed through the following equation:

$$\partial_\theta(\Re\psi) |_{\theta=\theta_{max}} = 0 \quad (4.42)$$

where $\theta_{max} = \arg \max_\theta |\psi_0|^2$, i.e. the position of the maximum of ψ_0 , the initial guess solution. The equation requires that the solution¹² must have a critical point in the fixed position θ_{max} . In this way we obtain the following system of equations:

$$\begin{cases} -(1 + i(\zeta_0 - \frac{1}{2}\partial_\theta^2))\psi + i\psi(1 - \tau\partial_\theta)|\psi|^2 + f - ia_{\bar{\mu}}\psi_{\bar{\mu}}e^{i\bar{\mu}\theta} + v_g\partial_\theta\psi = 0 \\ -(1 - i(\zeta_0 - \frac{1}{2}\partial_\theta^2))\psi^* - i\psi^*(1 - \tau\partial_\theta)|\psi|^2 + f + ia_{\bar{\mu}}\psi_{\bar{\mu}}^*e^{-i\bar{\mu}\theta} + v_g\partial_\theta\psi^* = 0 \\ \partial_\theta(\Re\psi) |_{\theta=\theta_{max}} = 0 \end{cases} \quad (4.43)$$

¹²Actually for convenience only the real part has been considered, but it is equivalent due to the independence of real and imaginary part of ψ

4.4.2 Matrix Form of the Equations

To be able to implement the method it is convenient to formally rewrite this system of equations in a matrix-like equation of the form¹³:

$$\underline{\hat{A}} \underline{\Phi}' = 0 \quad (4.44)$$

To do so we first notice that formally it possible to rewrite equation (4.39) as a matrix product between a so defined row vector and the solution vector as follows¹⁴:

$$\hat{r}_1 \underline{\Phi}' := \begin{bmatrix} -1 - i(\zeta_0 - \frac{1}{2}\partial_\theta^2 + a_{\bar{\mu}} \int d\theta e^{i\bar{\mu}(\theta' - \theta)}) \\ i\psi^2(1 - \tau\partial_\theta) - i\tau\psi\partial_\theta\psi \\ \partial_\theta\psi \end{bmatrix}^\top \begin{bmatrix} \psi \\ \psi^* \\ v_g \end{bmatrix} = 0 \quad (4.45)$$

Analogous reasoning can be applied to express the second equation in (4.43) as follows: :

$$\hat{r}_2 \underline{\Phi}' := \begin{bmatrix} -i\psi^{*2}(1 - \tau\partial_\theta) + i\tau\psi^*\partial_\theta\psi^* \\ -1 + i(\zeta_0 - \frac{1}{2}\partial_\theta^2 + a_{\bar{\mu}} \int d\theta e^{i\bar{\mu}(\theta' - \theta)}) \\ \partial_\theta\psi^* \end{bmatrix}^\top \begin{bmatrix} \psi \\ \psi^* \\ v_g \end{bmatrix} = 0 \quad (4.46)$$

For the third equation we need further considerations to be done. We can formally rewrite it as follows:

$$\partial_\theta(\Re\psi)|_{\theta=\theta_{max}} = \int_{\mathcal{R}} d\theta\delta(\theta - \theta_{max})\partial_\theta(\Re\psi) = \frac{1}{2} \int_{\mathcal{R}} d\theta\delta(\theta - \theta_{max})\partial_\theta(\psi + \psi^*) \quad (4.47)$$

$$= \frac{1}{2} \int_{\mathcal{R}} d\theta\delta(\theta - \theta_{max})\partial_\theta(\psi + \psi^*) = \frac{1}{2} \int_{\mathcal{R}} d\theta\delta(\theta - \theta_{max})\mathcal{F}^{-1}\{i\mu\mathcal{F}\{\psi + \psi^*\}\} \quad (4.48)$$

¹³Note that this is a formal equation where the matrix $\underline{\hat{A}}$ can be a matrix of operators in principle depending on $\underline{\Phi}'$

¹⁴To do so the Raman term and the periodic perturbation have been rewritten as follows:

$$\begin{aligned} -i\tau\psi\partial_\theta|\psi|^2 &= -i\tau\psi^2\partial_\theta\psi^* - i\tau|\psi|^2\partial_\theta\psi \\ -ia_{\bar{\mu}}\psi_{\bar{\mu}}e^{i\bar{\mu}\theta'} &= -ia_{\bar{\mu}} \int d\theta e^{i\bar{\mu}(\theta' - \theta)}\psi(\theta) \end{aligned}$$

Where the integral has to be intended in the ring and for \mathcal{F} and \mathcal{F}^{-1} the operator that respectively Fourier transforms and antitransforms an \mathcal{L}^2 function. In particular \mathcal{F}^{-1} acts on functions of the variable μ giving as an output a function of variable θ and conversely \mathcal{F} acts on functions of the variable θ giving as an output a function of variable μ . The last equivalence is obtained recalling that the action of the differential operator on the Fourier basis is represented by the multiplication of a factor $i\mu$.¹⁵

In this way we can formally rewrite the equation as:

$$\hat{\underline{\Gamma}}_3 \underline{\Phi}' := \begin{bmatrix} \frac{1}{2} \int_{\mathcal{R}} d\theta \delta(\theta - \theta_{max}) i\mathcal{F}^{-1} \mu \mathcal{F} \\ \frac{1}{2} \int_{\mathcal{R}} d\theta \delta(\theta - \theta_{max}) i\mathcal{F}^{-1} \mu \mathcal{F} \\ 0 \end{bmatrix}^\top \begin{bmatrix} \psi \\ \psi^* \\ v_g \end{bmatrix} = 0 \quad (4.49)$$

That allows us to formally define the following matricial operator as:

$$\hat{\underline{\Gamma}}(\psi, \psi^*) := \begin{bmatrix} \hat{\Gamma}_1 \\ \hat{\Gamma}_2 \\ \hat{\Gamma}_3 \end{bmatrix} \equiv \begin{bmatrix} -1 - i(\zeta_0 - \frac{1}{2}\partial_\theta^2 + a_{\bar{\mu}} \int d\theta e^{i\bar{\mu}(\theta' - \theta)}) & i\psi^2(1 - \tau\partial_\theta) - i\tau\psi\partial_\theta\psi & \partial_\theta\psi \\ -i\psi^{*2}(1 - \tau\partial_\theta) + i\tau\psi^*\partial_\theta\psi^* & -1 + i(\zeta_0 - \frac{1}{2}\partial_\theta^2 + a_{\bar{\mu}} \int d\theta e^{i\bar{\mu}(\theta' - \theta)}) & \partial_\theta\psi^* \\ \frac{1}{2} \int_{\mathcal{R}} d\theta \delta(\theta - \theta_{max}) i\mathcal{F}^{-1} \mu \mathcal{F} & \frac{1}{2} \int_{\mathcal{R}} d\theta \delta(\theta - \theta_{max}) i\mathcal{F}^{-1} \mu \mathcal{F} & 0 \end{bmatrix} \quad (4.51)$$

Finally the system of equations (4.43) is formally rewritten¹⁶:

$$\hat{\underline{\Gamma}}(\underline{\Phi}') \underline{\Phi}' = 0 \quad (4.52)$$

To compute now the Jacobian matrix operator apply the definition (4.31) to the system (4.43) expressing it in vectorial form:

$$\begin{bmatrix} -(1 + i(\zeta_0 - \frac{1}{2}\partial_\theta^2))\psi + i\psi(1 - \tau\partial_\theta)|\psi|^2 + f - ia_{\bar{\mu}}\psi_{\bar{\mu}}e^{i\bar{\mu}\theta} + v_g\partial_\theta\psi \\ -(1 - i(\zeta_0 - \frac{1}{2}\partial_\theta^2))\psi^* - i\psi^*(1 - \tau\partial_\theta)|\psi|^2 + f + ia_{\bar{\mu}}\psi_{\bar{\mu}}^*e^{-i\bar{\mu}\theta} + v_g\partial_\theta\psi^* \\ \partial_\theta(\Re\psi)|_{\theta=\theta_{max}} \end{bmatrix} = 0 \quad (4.53)$$

¹⁵This is at the basis of the solution of linear PDE through the Fourier transform

¹⁶To note that all the integrals present in the matrix has to be considered as integral operators, defined just when applied to a specific function

Obtaining:

$$\underline{\hat{J}}(\Phi) = \begin{bmatrix} \hat{j}_1 & \hat{j}_2 & \hat{j}_3 \end{bmatrix} \quad (4.54)$$

where with \hat{j}_i we indicate the i -th column of the matricial operator, defined as follows:

$$\hat{j}_1 = \begin{bmatrix} -1 - i(\zeta_0 - \frac{1}{2}\partial_\theta^2 + a_{\bar{\mu}} \int d\theta e^{i\bar{\mu}(\theta' - \theta)} - 2|\psi|^2) + v_g \partial_\theta - i\tau(\{\partial_\theta, |\psi|^2\} + \psi \partial_\theta \psi^*) \\ -i\psi^{*2}(1 - \tau \partial_\theta) + i\tau \psi^* \partial_\theta \psi^* \\ \frac{1}{2} \int_{\mathcal{R}} d\theta \delta(\theta - \theta_{max}) i\mathcal{F}^{-1} \mu \mathcal{F} \end{bmatrix} \quad (4.55)$$

$$\hat{j}_2 = \begin{bmatrix} i\psi^2(1 - \tau \partial_\theta) - i\tau \psi \partial_\theta \psi \\ -1 + i(\zeta_0 - \frac{1}{2}\partial_\theta^2 + a_{\bar{\mu}} \int d\theta e^{-i\bar{\mu}(\theta' - \theta)} - 2|\psi|^2) + v_g \partial_\theta - i\tau(\{\partial_\theta, |\psi|^2\} + \psi^* \partial_\theta \psi) \\ \frac{1}{2} \int_{\mathcal{R}} d\theta \delta(\theta - \theta_{max}) i\mathcal{F}^{-1} \mu \mathcal{F} \end{bmatrix} \quad (4.56)$$

$$\hat{j}_3 = \begin{bmatrix} \partial_\theta \psi \\ \partial_\theta \psi^* \\ 0 \end{bmatrix} \quad (4.57)$$

Noticing the similarities with (4.51), the Jacobian can be rewritten as:

$$\underline{\hat{J}}(\psi, \psi^*) = \underline{\hat{F}}(\psi, \psi^*) + \begin{bmatrix} \hat{\Delta}(\psi, \psi^*) & 0 & 0 \\ 0 & \hat{\Delta}^*(\psi, \psi^*) & 0 \\ 0 & 0 & 0 \end{bmatrix} \quad (4.58)$$

Where $\hat{\Delta}(\psi, \psi^*) := 2i|\psi|^2 + v_g \partial_\theta - i\tau(\partial_\theta |\psi|^2 + |\psi|^2 \partial_\theta + \psi \partial_\theta \psi^*)$

4.4.3 Discretization of the Equations

Once we defined the equations and the variables of our problem, we can now describe how to discretize it in order to run the algorithm on a computer program.

Let us start from the solution array $\underline{\Phi}'$, and in particular on its continuous components (i.e. ψ and ψ^*).

Considered N the size of the discretization of the field ψ , we can associate to the latter the following array¹⁷:

$$\psi \rightarrow \underline{\psi} := \sum_{i=1}^N \psi_i \hat{e}_i \quad (4.59)$$

¹⁷With \hat{e}_i we consider the i -th unit versor of \mathbb{C}^{2N+1} that is the space in which the discretized solution $\underline{\Phi}'$ lives

We can then write the discretised version of the solution array $\underline{\Phi}'$ as:

$$\underline{\Phi}' \rightarrow \underline{\Phi} := \sum_{i=1}^{2N+1} \Phi_i \hat{e}_i \quad (4.60)$$

where:

$$\Phi_i = \begin{cases} \psi_i & i < N + 1 \\ \psi_i^* & N < i < 2N + 1 \\ v_g & i = 2N + 1 \end{cases} \quad (4.61)$$

After having discretized the vector solution, also the system of equations (4.43) have to be expressed in the discretized form a matricial equation of the form (4.33).

First of all we notice that, since in the discretized formulation we have $2N+1$ unknowns, we need to expand also the number of equations. Noticing that each entry of (4.51) or (4.58), indexed with $i < 3$ or $j < 3$ is related to the scalar fields ψ , ψ^* , that have been already discretized in N -dimensional vectors, it is possible to expand the number of equations converting the two 3×3 -matricial operators (4.51)(4.58) in two $2N + 1 \times 2N + 1$ scalar matrices $\underline{\underline{F}}(\underline{\Phi}), \underline{\underline{J}}(\underline{\Phi}) \in \mathbb{C}^{2N+1 \times 2N+1}$, whose entries depend on the solution vector¹⁸ $\underline{\Phi}$.

Decomposing $\hat{\underline{\underline{F}}}(\underline{\Phi})$ and $\hat{\underline{\underline{J}}}(\underline{\Phi})$ as follows:

$$\hat{\underline{\underline{F}}}(\underline{\Phi}) = \underline{\underline{A}}^F(\underline{\Phi}) + \hat{\underline{\underline{O}}}^F(\underline{\Phi}) \quad (4.62)$$

$$\hat{\underline{\underline{J}}}(\underline{\Phi}) = \underline{\underline{A}}^J(\underline{\Phi}) + \hat{\underline{\underline{O}}}^J(\underline{\Phi}) \quad (4.63)$$

Where $\underline{\underline{A}}^I(\underline{\Phi})$ represents the scalar part of the original matrix and $\hat{\underline{\underline{O}}}^I(\underline{\Phi})$ its operatorial part, $I \in \{F, J\}$.

In term of discretization, for the scalar part of both operator (4.51)(4.58) it can be done straightforwardly according to the following procedure:

being $A_{i,j}^I(\psi, \psi^*)$ an entry of the scalar part of (4.51) or (4.58) ($I = F$ and $I = J$ respectively), with $i < 3 \wedge j < 3$, we will associate to it a complex matrix defined as follows:

$$A_{i,j}^I(\psi(\theta), \psi^*(\theta)) \rightarrow \underline{\underline{M}}^{I,i,j}(\underline{\Phi}) := \sum_{n=1}^N A_{i,j}^I(\psi_n, \psi_n^*) \hat{e}_n \hat{e}_n^\top \quad (4.64)$$

¹⁸This does not result in a problem since, as prescribed by the method, at any iteration they will be computed at the value of the preceding iteration

That is a $N \times N$ diagonal matrix having in each non vanishing component the entry of the original matrix computed at a given point of the discretization grid.

With analogous reasoning, the third column of both the matrix operators (4.51) and (4.58) (for both equal to \hat{j}_3), not depending on any operator, can be readily extended to obtain the $(2N+1)$ -th column of the discretized scalar $2N+1 \times 2N+1$ matrices ($\underline{\underline{F}}(\Phi)$ or $\underline{\underline{J}}(\Phi)$) as:

$$\hat{j}_3 = \begin{bmatrix} \partial_\theta \psi \\ \partial_\theta \psi^* \\ 0 \end{bmatrix} \rightarrow \underline{\underline{c}}_{2N+1}^I(\Phi) := \sum_{n=1}^{2N+1} a_n \hat{e}_n \quad (4.65)$$

With:

$$a_n = \begin{cases} (\partial_\theta \psi)_n & n < N+1 \\ (\partial_\theta \psi^*)_n & N < n < 2N+1 \\ 0 & n = 2N+1 \end{cases} \quad (4.66)$$

To finally implement also the operatorial parts of (4.51) and (4.58), represented by the differential or integral operators, we exploit the python function "sp.linalg.dft" implementing the Discrete Fourier Transform through the so called DFT matrix[49] This matrix and its inverse are exactly the discrete implementation of the operators presented in (4.48), that make possible to write a differential (or integral operator) by explicitly writing its algebraic counterpart in the Fourier space. In such a way, we were able to compute both the remaining operatorial terms $\underline{\underline{\hat{O}}}^F$ and $\underline{\underline{\hat{O}}}^J$. In this way we can readily write the matrix representation of the family of operators ∂_θ^n .

Being $\underline{\underline{\mathcal{F}}}$ the N points DFT matrix, the matrix associated to ∂_θ^n is found as follows:

$$\partial_\theta^n \psi \rightarrow \underline{\underline{\mathcal{F}}}^{-1}((i\mu)^n) \underline{\underline{\mathcal{F}}} \psi \quad (4.67)$$

where $\underline{\underline{\mathcal{D}}}^n := \underline{\underline{\mathcal{F}}}^{-1}(i\mu^n) \underline{\underline{\mathcal{F}}}$ is the searched matrix.

And analogously for the integral term in the diagonal entries of \hat{F} :

$$-a_{\bar{\mu}} \mathcal{F} \int d\theta \psi(\theta) e^{i\bar{\mu}(\theta' - \theta)} = -a_{\bar{\mu}} \psi_{\bar{\mu}} \mathcal{F} e^{i\bar{\mu}\theta'} = -a_{\bar{\mu}} \delta_{\mu, \bar{\mu}} \mathcal{F} \psi \rightarrow -a_{\bar{\mu}} \delta_{\mu, \bar{\mu}} \underline{\underline{\mathcal{F}}} \psi \quad (4.68)$$

A last consideration is required for the discretization of (4.48).

As the δ -function select a particular point in the continuous space θ , also in the discretization it is required to take a single value of the discretized derivative and this is readily implemented as follows:

$$\frac{1}{2} \int_{\mathcal{R}} d\theta \delta(\theta - \theta_{max}) \mathcal{F}^{-1} \{ i\mu \mathcal{F} \{ \psi \} \} \rightarrow \frac{1}{2} \hat{e}_{n_{max}}^\top \underline{\underline{\mathcal{F}}}^{-1}(i\mu) \underline{\underline{\mathcal{F}}} \quad (4.69)$$

Where only the n_{max} -row of the matrix $\underline{\underline{\mathcal{F}}}^{-1}(i\mu)\underline{\underline{\mathcal{F}}}$ has been taken.

Finally, the discretized scalar matrices $\underline{\underline{F}}(\Phi)$ and $\underline{\underline{J}}(\Phi)$ have the following expression:

$$\underline{\underline{F}}(\Phi) = \begin{bmatrix} M^{F,1,1} & M^{F,1,2} \\ M^{F,2,1} & M^{F,2,2} & \underline{\underline{\mathcal{C}}}_{2N+1}^J(\Phi) \\ 0 & 0 & 0 \end{bmatrix} + \quad (4.70)$$

$$\begin{bmatrix} -i\underline{\underline{\mathcal{F}}}^{-1} \left(\frac{\mu^2}{2} + a_{\bar{\mu}}\delta_{\mu,\bar{\mu}} \right) \underline{\underline{\mathcal{F}}} & -i\tau \left(\sum_{n=1}^N \psi_n^2 \hat{e}_n \hat{e}_n^\top \right) \underline{\underline{\mathcal{D}}}^1 & 0 \\ i\tau \left(\sum_{n=1}^N \psi_n^{*2} \hat{e}_n \hat{e}_n^\top \right) \underline{\underline{\mathcal{D}}}^1 & i\underline{\underline{\mathcal{F}}}^{-1} \left(\frac{\mu^2}{2} + a_{\bar{\mu}}\delta_{\mu,\bar{\mu}} \right) \underline{\underline{\mathcal{F}}} & 0 \\ \frac{1}{2} \hat{e}_{n_{max}}^\top \underline{\underline{\mathcal{D}}}^1 & \frac{1}{2} \hat{e}_{n_{max}}^\top \underline{\underline{\mathcal{D}}}^1 & 0 \end{bmatrix} \quad (4.71)$$

$$(4.72)$$

$$\underline{\underline{J}}(\Phi) = \underline{\underline{F}}(\Phi) + \begin{bmatrix} \underline{\underline{\Delta}}(\Phi) & 0 & 0 \\ 0 & (\underline{\underline{\Delta}}(\Phi))^* & 0 \\ 0 & 0 & 0 \end{bmatrix} \quad (4.73)$$

Where:

$$M^{F,1,1} = -(1 + i\zeta_0)\underline{\underline{\mathbb{I}}} \quad (4.74)$$

$$M^{F,1,2} = i \sum_{n=1}^N \psi_n^2 \hat{e}_n \hat{e}_n^\top \quad (4.75)$$

$$M^{F,2,1} = -i \sum_{n=1}^N \psi_n^{*2} \hat{e}_n \hat{e}_n^\top \quad (4.76)$$

$$M^{F,2,2} = (-1 + i\zeta_0)\underline{\underline{\mathbb{I}}} \quad (4.77)$$

$$(4.78)$$

and:

$$\begin{aligned} \underline{\underline{\Delta}}(\Phi) := & i \sum_{n=1}^N (2|\psi_n|^2 + \tau((\partial_\theta |\psi|^2)_n) + \psi_n (\partial_\theta \psi^*)_n) \hat{e}_n \hat{e}_n^\top + \\ & - i\tau \left(\sum_{n=1}^N |\psi_n|^2 \hat{e}_n \hat{e}_n^\top \right) \underline{\underline{\mathcal{D}}}^1 \end{aligned} \quad (4.79)$$

4.4.4 Initialization condition

Once all the operators are written in terms of scalar matrices and so implementable in the discrete architecture of the computer, the remaining step to apply the method described in (4.32) is the definition of the the initial condition.

As initial condition we have taken the soliton solution obtained from the split-step method above described, and on this point is important to highlight some

considerations.

We remind that the aim of the implementation of this method is that of speeding up the computation of the group velocity acquired by the system in an extended region of the subspace of the parameters space related to the perturbation parameters and to the detuning, i.e. on the subspace $(a_{\bar{\mu}}, \bar{\mu}, \zeta_0)$, in place of using the split-step method that, simulating the whole dynamics of the system, requires a longer computation time.

If we assume so to take as initial condition a different result of the split-step method it will require to first simulate the system with split-step for later applying the Newton-Raphson method, resulting still in a very long computation time required. To overcome this situation, a single hard seed has been taken to initiate the Newton-Raphson method. In this way, after the simulation for the first operating point has been terminated we took the converged solution to seed the next simulation, obtaining a two-fold advantage, speeding up the computation and insuring that the seed is always close enough to the actual solution associated to the new operating point.

This procedure is valid since we scanned the parameter space in a way that two subsequent applications of the method were related to close points in the parameter space.

Chapter 5

Conclusions and outlook.

In this work, we proposed a model of the perturbed Lugiato-Lefever equation that can catch the main physics of soliton dynamics in the presence of the avoided mode crossing in Kerr microresonators. We studied the main properties of the model obtaining insights about the formation of the dispersive waves in the resonator and their impact on the soliton dynamics.

Our starting point has been a recent experimental study [29] showing that the presence of the avoided mode crossing can lead to the phenomenon of noise suppression in rings microresonators - crucial property to use this system that can be used in various applications. To deepen the understanding of this phenomenon, we derived a new model, we further extended the model to take into account the presence of phase noise of the driving laser. We provided versatile studies of the system considering first the effect of the mode crossing alone, next the effect of Raman scattering, and finally both these effects together. Thus, we have proven that the complete model effectively demonstrates the reduction of the noise transduction to the soliton repetition rate. We verified that this is possible for a given operating point of the system (referred in literature as quiet point). Furthermore, we applied a fast simulation approach (known as Newton-Raphson method) to explore wider regions of the parameters space, finding out, for the first time in literature, that the quiet point is not a unique point related to a specific avoided mode crossing geometry, but it can be obtained, in principle, within different dispersion profiles. We finally justified these numerical results through an analytical derivation that, after additional improvements, could in principle lead to an a priori prediction of the position of the quiet points in the whole soliton existence range.

We underline that, at the moment, the present work is still theoretical and that must be proven by subsequent experimental studies. Thus, as the outlook of the study, we would like to highlight the unique possibilities that follow after the experimental implementation of an integrated device that can perform an active scan over the quiet point parameter space. One of such possibilities can be the

significant miniaturization of a very low-noise yet compact RF source that can be, for instance, easily placed in a space shuttle saving valuable cargo weight. However, the realization of such a device remains a very challenging task that nonetheless can be achieved in the nearest future. Indeed, the Laboratory of Photonics and Quantum Measurements at EPFL is actively testing different schemes and implementations to make these ideas a reality. In this regard, the results obtained in this thesis can serve as a solid theoretical foundation for identifying all the criteria to reach the thermodynamical noise limit in the soliton generating cavities.

Bibliography

- [1] T. Herr, V. Brasch, J. D. Jost, C. Y. Wang, N. M. Kondratiev, M. L. Gorodetsky, and T. J. Kippenberg. «Temporal solitons in optical microresonators». In: *Nature Photonics* 8.2 (Dec. 2013), pp. 145–152. DOI: 10.1038/nphoton.2013.343. URL: <https://doi.org/10.1038%5C%2Fnphoton.2013.343> (cit. on pp. 1, 4, 5).
- [2] Tobias J. Kippenberg, Alexander L. Gaeta, Michal Lipson, and Michael L. Gorodetsky. «Dissipative Kerr solitons in optical microresonators». In: *Science* 361.6402 (2018), eaan8083. DOI: 10.1126/science.aan8083. eprint: <https://www.science.org/doi/pdf/10.1126/science.aan8083>. URL: <https://www.science.org/doi/abs/10.1126/science.aan8083> (cit. on pp. 1–3, 5).
- [3] J. D. Jost, T. Herr, C. Lecaplain, V. Brasch, M. H. P. Pfeiffer, and T. J. Kippenberg. «Counting the cycles of light using a self-referenced optical microresonator». In: *Optica* 2.8 (Aug. 2015), p. 706. DOI: 10.1364/optica.2.000706. URL: <https://doi.org/10.1364%5C%2FOptica.2.000706> (cit. on p. 1).
- [4] Victor Brasch, Erwan Lucas, John D Jost, Michael Geiselmann, and Tobias J Kippenberg. «Self-referenced photonic chip soliton Kerr frequency comb». In: *Light: Science & Applications* 6.1 (Aug. 2016), e16202–e16202. DOI: 10.1038/lsa.2016.202. URL: <https://doi.org/10.1038%5C%2Flsa.2016.202> (cit. on p. 1).
- [5] Daryl T. Spencer et al. «An Integrated-Photonics Optical-Frequency Synthesizer». In: (2017). DOI: 10.48550/ARXIV.1708.05228. URL: <https://arxiv.org/abs/1708.05228> (cit. on p. 1).
- [6] Pablo Marin-Palomo et al. «Microresonator-based solitons for massively parallel coherent optical communications». In: *Nature* 546.7657 (June 2017), pp. 274–279. DOI: 10.1038/nature22387. URL: <https://doi.org/10.1038%5C%2Fnature22387> (cit. on p. 1).

- [7] Ian Coddington, Nathan Newbury, and William Swann. «Dual-comb spectroscopy». In: *Optica* 3.4 (Apr. 2016), p. 414. DOI: 10.1364/optica.3.000414. URL: <https://doi.org/10.1364%5C%2Foptica.3.000414> (cit. on p. 1).
- [8] P. Trocha et al. «Ultrafast optical ranging using microresonator soliton frequency combs». In: *Science* 359.6378 (2018), pp. 887–891. DOI: 10.1126/science.aao3924. eprint: <https://www.science.org/doi/pdf/10.1126/science.aao3924>. URL: <https://www.science.org/doi/abs/10.1126/science.aao3924> (cit. on p. 1).
- [9] Myoung-Gyun Suh and Kerry Vahala. «Soliton Microcomb Range Measurement». In: (2017). DOI: 10.48550/ARXIV.1705.06697. URL: <https://arxiv.org/abs/1705.06697> (cit. on p. 1).
- [10] Scott B. Papp, Katja Beha, Pascal Del’Haye, Franklyn Quinlan, Hansuek Lee, Kerry J. Vahala, and Scott A. Diddams. «Microresonator frequency comb optical clock». In: *Optica* 1.1 (July 2014), p. 10. DOI: 10.1364/optica.1.000010. URL: <https://doi.org/10.1364%5C%2Foptica.1.000010> (cit. on p. 1).
- [11] E. Obrzud et al. *A Microphotonic Astrocomb*. 2017. DOI: 10.48550/ARXIV.1712.09526. URL: <https://arxiv.org/abs/1712.09526> (cit. on p. 1).
- [12] Myoung-Gyun Suh et al. «Searching for Exoplanets Using a Microresonator Astrocomb». In: (2018). DOI: 10.48550/ARXIV.1801.05174. URL: <https://arxiv.org/abs/1801.05174> (cit. on p. 1).
- [13] Govind P. Agrawal. *Nonlinear Fiber Optics*. Springer Berlin Heidelberg, pp. 195–211. DOI: 10.1007/3-540-46629-0_9. URL: [%5Curl%7Bhttps://doi.org/10.1007%5C%2F3-540-46629-0_9%7D](https://doi.org/10.1007%5C%2F3-540-46629-0_9) (cit. on pp. 3, 4, 7).
- [14] Yanne K. Chembo and Nan Yu. «Modal expansion approach to optical-frequency-comb generation with monolithic whispering-gallery-mode resonators». In: *Physical Review A* 82.3 (Sept. 2010). DOI: 10.1103/physreva.82.033801. URL: <https://doi.org/10.1103%5C%2Fphysreva.82.033801> (cit. on pp. 4, 7, 25).
- [15] Yanne K. Chembo and Curtis R. Menyuk. «Spatiotemporal Lugiato-Lefever formalism for Kerr-comb generation in whispering-gallery-mode resonators». In: *Physical Review A* 87.5 (May 2013). DOI: 10.1103/physreva.87.053852. URL: <https://doi.org/10.1103%5C%2Fphysreva.87.053852> (cit. on pp. 4, 5, 7, 18, 25, 26).
- [16] L. A. Lugiato and R. Lefever. «Spatial Dissipative Structures in Passive Optical Systems». In: *Physical Review Letters* 58.21 (May 1987), pp. 2209–2211. DOI: 10.1103/physrevlett.58.2209. URL: <https://doi.org/10.1103%5C%2Fphysrevlett.58.2209> (cit. on p. 4).

- [17] Zhen Qi, Shaokang Wang, José Jaramillo-Villegas, Minghao Qi, Andrew M. Weiner, Giuseppe D’Aguanno, Thomas F. Carruthers, and Curtis R. Menyuk. «Dissipative cnoidal waves (Turing rolls) and the soliton limit in microring resonators». In: *Optica* 6.9 (Sept. 2019), pp. 1220–1232. DOI: 10.1364/OPTICA.6.001220. URL: <http://opg.optica.org/optica/abstract.cfm?URI=optica-6-9-1220> (cit. on p. 5).
- [18] Saliya Coulibaly, Majid Taki, Abdelkrim Bendahmane, Guy Millot, Bertrand Kibler, and Marcel Gabriel Clerc. «Turbulence-Induced Rogue Waves in Kerr Resonators». In: *Phys. Rev. X* 9 (1 Mar. 2019), p. 011054. DOI: 10.1103/PhysRevX.9.011054. URL: <https://link.aps.org/doi/10.1103/PhysRevX.9.011054> (cit. on p. 5).
- [19] E. Lucas, M. Karpov, H. Guo, M. L. Gorodetsky, and T. J. Kippenberg. «Breathing dissipative solitons in optical microresonators». In: *Nature Communications* 8.1 (Sept. 2017). DOI: 10.1038/s41467-017-00719-w. URL: <https://doi.org/10.1038/s41467-017-00719-w> (cit. on p. 5).
- [20] Cyril Godey, Irina V. Balakireva, Aurélien Coillet, and Yanne K. Chembo. «Stability analysis of the spatiotemporal Lugiato-Lefever model for Kerr optical frequency combs in the anomalous and normal dispersion regimes». In: *Phys. Rev. A* 89 (6 June 2014), p. 063814. DOI: 10.1103/PhysRevA.89.063814. URL: <https://link.aps.org/doi/10.1103/PhysRevA.89.063814> (cit. on pp. 5–7).
- [21] Tobias Herr, Michael L. Gorodetsky, and Tobias J. Kippenberg. *Dissipative Kerr solitons in optical microresonators*. 2015. DOI: 10.48550/ARXIV.1508.04989. URL: <https://arxiv.org/abs/1508.04989> (cit. on p. 5).
- [22] Lucas, Erwan Guillaume Albert. «Physics of Dissipative Kerr Solitons in Optical Microresonators and Application to Frequency Synthesis». en. In: (2019). DOI: 10.5075/EPFL-THESIS-9109. URL: https://infoscience.epfl.ch/record/267490/files/EPFL_TH9109.pdf (cit. on p. 6).
- [23] T. Herr, V. Brasch, J. D. Jost, I. Mirgorodskiy, G. Lihachev, M. L. Gorodetsky, and T. J. Kippenberg. «Mode Spectrum and Temporal Soliton Formation in Optical Microresonators». In: *Phys. Rev. Lett.* 113 (12 Sept. 2014), p. 123901. DOI: 10.1103/PhysRevLett.113.123901. URL: <https://link.aps.org/doi/10.1103/PhysRevLett.113.123901> (cit. on pp. 6–8).
- [24] Erwan Lucas, Hairun Guo, John D. Jost, Maxim Karpov, and Tobias J. Kippenberg. «Detuning-dependent properties and dispersion-induced instabilities of temporal dissipative Kerr solitons in optical microresonators». In: *Phys. Rev. A* 95 (4 Apr. 2017), p. 043822. DOI: 10.1103/PhysRevA.95.043822. URL: <https://link.aps.org/doi/10.1103/PhysRevA.95.043822> (cit. on p. 7).

-
- [25] Tal Carmon, Harald G. L. Schwefel, Lan Yang, Mark Oxborrow, A. Douglas Stone, and Kerry J. Vahala. «Static Envelope Patterns in Composite Resonances Generated by Level Crossing in Optical Toroidal Microcavities». In: *Phys. Rev. Lett.* 100 (10 Mar. 2008), p. 103905. DOI: 10.1103/PhysRevLett.100.103905. URL: <https://link.aps.org/doi/10.1103/PhysRevLett.100.103905> (cit. on p. 7).
- [26] A. A. Savchenkov, A. B. Matsko, W. Liang, V. S. Ilchenko, D. Seidel, and L. Maleki. «Kerr frequency comb generation in overmoded resonators». In: *Opt. Express* 20.24 (Nov. 2012), pp. 27290–27298. DOI: 10.1364/OE.20.027290. URL: <http://opg.optica.org/oe/abstract.cfm?URI=oe-20-24-27290> (cit. on p. 7).
- [27] H.A. Haus and W. Huang. «Coupled-mode theory». In: *Proceedings of the IEEE* 79.10 (1991), pp. 1505–1518. DOI: 10.1109/5.104225 (cit. on p. 7).
- [28] Hairun Guo, Erwan Lucas, Martin HP Pfeiffer, Maxim Karpov, Miles Anderson, Junqiu Liu, Michael Geiselmann, John D Jost, and Tobias J Kippenberg. «Intermode breather solitons in optical microresonators». In: *Phys. Rev. X* 7.4 (2017), p. 041055 (cit. on p. 8).
- [29] Xu Yi, Qi-Fan Yang, Xueyue Zhang, Ki Youl Yang, Xinbai Li, and Kerry Vahala. «Single-mode dispersive waves and soliton microcomb dynamics». In: *Nature Communications* 8.1 (Mar. 2017). DOI: 10.1038/ncomms14869. URL: <https://doi.org/10.1038%5C%2Fncmms14869> (cit. on pp. 9, 11, 25, 61).
- [30] Xiaoxiao Xue, Yi Xuan, Yang Liu, Pei-Hsun Wang, Steven Chen, Jian Wang, Dan E Leaird, Minghao Qi, and Andrew M Weiner. «Mode-locked dark pulse Kerr combs in normal-dispersion microresonators». In: *Nat. Photonics* 9.9 (2015), p. 594. DOI: <https://doi.org/10.1038/nphoton.2015.137> (cit. on p. 9).
- [31] Xiaoxiao Xue, Yi Xuan, Pei-Hsun Wang, Yang Liu, Dan E Leaird, Minghao Qi, and Andrew M Weiner. «Normal-dispersion microcombs enabled by controllable mode interactions». In: *Laser Photonics Rev.* 9.4 (2015), pp. L23–L28 (cit. on p. 9).
- [32] Bok Young Kim, Yoshitomo Okawachi, Jae K Jang, Mengjie Yu, Xingchen Ji, Yun Zhao, Chaitanya Joshi, Michal Lipson, and Alexander L Gaeta. «Turnkey, high-efficiency Kerr comb source». In: *Opt. Lett.* 44.18 (2019), pp. 4475–4478 (cit. on p. 9).
- [33] Oskar B. Helgason, Francisco R. Arteaga-Sierra, Zhichao Ye, Krishna Twayana, P. A. Andrekson, Magnus Karlsson, Jochen Schroder, and Víctor Torres-Company. «Dissipative Kerr solitons in photonic molecules». In: *arXiv preprint arXiv:2007.02608* (2020) (cit. on p. 9).

- [34] Maxim Karpov, Martin HP Pfeiffer, Hairun Guo, Wenle Weng, Junqiu Liu, and Tobias J Kippenberg. «Dynamics of soliton crystals in optical microresonators». In: *Nat. Phys.* 15.10 (2019), pp. 1071–1077. DOI: <https://doi.org/10.1038/s41567-019-0635-0> (cit. on p. 9).
- [35] Andrey B. Matsko, Wei Liang, Anatoliy A. Savchenkov, Danny Eliyahu, and Lute Maleki. «Optical Cherenkov radiation in overmoded microresonators». In: *Opt. Lett.* 41.13 (July 2016), pp. 2907–2910. DOI: 10.1364/OL.41.002907. URL: <http://opg.optica.org/ol/abstract.cfm?URI=ol-41-13-2907> (cit. on pp. 11, 19).
- [36] Franz G. Mertens, Niurka R. Quintero, and A. R. Bishop. «Nonlinear Schrödinger equation with spatiotemporal perturbations». In: *Phys. Rev. E* 81 (1 Jan. 2010), p. 016608. DOI: 10.1103/PhysRevE.81.016608. URL: <https://link.aps.org/doi/10.1103/PhysRevE.81.016608> (cit. on pp. 14, 39, 41, 42).
- [37] Maxim Karpov, Martin H. P. Pfeiffer, Hairun Guo, Wenle Weng, Junqiu Liu, and Tobias J. Kippenberg. «Dynamics of soliton crystals in optical microresonators». In: *Nature Physics* 15.10 (Sept. 2019), pp. 1071–1077. DOI: 10.1038/s41567-019-0635-0. URL: <https://doi.org/10.1038/s41567-019-0635-0> (cit. on pp. 17, 21).
- [38] Su-Peng Yu, Daniel C. Cole, Hojoong Jung, Gregory T. Moille, Kartik Srinivasan, and Scott B. Papp. «Spontaneous pulse formation in edgeless photonic crystal resonators». In: *Nature Photonics* 15.6 (Apr. 2021), pp. 461–467. DOI: 10.1038/s41566-021-00800-3. URL: <https://doi.org/10.1038/s41566-021-00800-3> (cit. on p. 18).
- [39] Óskar B. Helgason, Marcello Girardi, Zhichao Ye, Fuchuan Lei, Jochen Schröder, and Victor Torres Company. *Power-efficient soliton microcombs*. 2022. DOI: 10.48550/ARXIV.2202.09410. URL: <https://arxiv.org/abs/2202.09410> (cit. on pp. 18, 19).
- [40] Andrey B. Matsko and Lute Maleki. «Noise conversion in Kerr comb RF photonic oscillators». In: *J. Opt. Soc. Am. B* 32.2 (Feb. 2015), pp. 232–240. DOI: 10.1364/JOSAB.32.000232. URL: <http://opg.optica.org/josab/abstract.cfm?URI=josab-32-2-232> (cit. on pp. 19, 24).
- [41] Yadong Wang, François Leo, Julien Fatome, Miro Erkintalo, Stuart G. Murdoch, and Stéphane Coen. «Universal mechanism for the binding of temporal cavity solitons». In: *Optica* 4.8 (Aug. 2017), pp. 855–863. DOI: 10.1364/OPTICA.4.000855. URL: <http://opg.optica.org/optica/abstract.cfm?URI=optica-4-8-855> (cit. on p. 19).

-
- [42] Guanhao Huang, Erwan Lucas, Junqiu Liu, Arslan S. Raja, Grigory Lihachev, Michael L. Gorodetsky, Nils J. Engelsen, and Tobias J. Kippenberg. «Thermorefractive noise in silicon-nitride microresonators». In: *Physical Review A* 99.6 (June 2019). DOI: 10.1103/physreva.99.061801. URL: <https://doi.org/10.1103/physreva.99.061801> (cit. on p. 24).
- [43] Fuchuan Lei, Zhichao Ye, Óskar B. Helgason, Attila Fülöp, Marcello Girardi, and Victor Torres-Company. «Optical linewidth of soliton microcombs». In: *Nature Communications* 13.1 (June 2022). DOI: 10.1038/s41467-022-30726-5. URL: <https://doi.org/10.1038/s41467-022-30726-5> (cit. on p. 24).
- [44] Maxim Karpov, Hairun Guo, Arne Kordts, Victor Brasch, Martin H. P. Pfeiffer, Michail Zervas, Michael Geiselmann, and Tobias J. Kippenberg. «Raman Self-Frequency Shift of Dissipative Kerr Solitons in an Optical Microresonator». In: *Physical Review Letters* 116.10 (Mar. 2016). DOI: 10.1103/physrevlett.116.103902. URL: <https://doi.org/10.1103/physrevlett.116.103902> (cit. on pp. 25, 29).
- [45] Junqiu Liu et al. «Photonic microwave generation in the X- and K-band using integrated soliton microcombs». In: *Nature Photonics* 14.8 (Apr. 2020), pp. 486–491. DOI: 10.1038/s41566-020-0617-x. URL: <https://doi.org/10.1038/s41566-020-0617-x> (cit. on pp. 25, 32).
- [46] Y. Kodama and A. Hasegawa. «Nonlinear pulse propagation in a monomode dielectric guide». In: *IEEE Journal of Quantum Electronics* 23.5 (May 1987), pp. 510–524. DOI: 10.1109/jqe.1987.1073392. URL: <https://doi.org/10.1109/jqe.1987.1073392> (cit. on p. 29).
- [47] Xu Yi, Qi-Fan Yang, Ki Youl Yang, and Kerry Vahala. «Theory and measurement of the soliton self-frequency shift and efficiency in optical microcavities». In: *Optics Letters* 41.15 (July 2016), p. 3419. DOI: 10.1364/ol.41.003419. URL: <https://doi.org/10.1364/ol.41.003419> (cit. on p. 42).
- [48] *Newton method*. https://en.wikipedia.org/wiki/Newton%27s_method (cit. on p. 51).
- [49] *Matrix Formulation of the DFT*. https://ccrma.stanford.edu/~jos/st/Matrix_Formulation_DFT.html (cit. on p. 58).